**Supplementary Information for "Far-field superresolution imaging via *k*-space superoscillation"**

Bohan Zhang[1], Hao Zhang[1], Fei Zhang[2], Wei Liu[3], Yuanmu Yang[1]*

[1]State Key Laboratory of Precision Measurement Technology and Instruments, Department of Precision Instrument, Tsinghua University, Beijing 100084, China

[2]National Key Laboratory of Optical Field Manipulation Science and Technology, Chinese Academy of Sciences, Chengdu 610209, China

[3]College for Advanced Interdisciplinary Studies, National University of Defense Technology, Changsha, Hunan 410073, China

* *Corresponding author*: ymyang@tsinghua.edu.cn

## 1 Cut-off frequency for an incoherent imaging system

For simplicity, we assume a far-field imaging condition with the object plane far from the aperture plane with the distance $l_o \gg D^2/\lambda$, where $\lambda$ is the illumination wavelength and $D$ is the aperture diameter. The range of the change rate of the transmitted field on the lens output plane with respect to the transverse wavenumber $k_x$ of the incident plane wave is from $W_{min}$ to $W_{max}$.

The local change rate can provide a good indication of where significant values of the Fourier spectrum will occur [1]. The range of the change rate of the complex amplitude field transmissible through the lens on the aperture plane is from $W_{min}$ to $W_{max}$ due to the linearity of the transmission function. Because the change rate with respect to $k_x$ at position $x$ on the aperture plane is $x$ for the incident plane wave $e^{jk_x x}$, the imaging system equivalently receives the wavefront on the aperture plane within the range $W_{min}$ to $W_{max}$. Due to the Fourier transform relationship between the complex amplitude field on the object plane and the aperture plane, the imaging system can receive the object's spatial frequencies in the range from $W_{min}/\lambda l_o$ to

$W_{max}/\lambda l_o$. This range corresponds to the bandwidth of the coherent transfer function, which equals the cut-off frequency of an incoherent imaging system. Therefore, the cut-off frequency of an incoherent imaging system corresponds to the difference between the maximum and minimum change rates of the transmitted field on the lens output plane with respect to $k_x$.

## 2 Role of nonlocality in superresolution imaging via *k*-space superoscillation

Under Fresnel approximation, the incident plane wave $e^{jk_x x}$ is modulated by a local element with angle-independent transmission $t_1(x)$. After propagation of distance $z$, the diffraction field of the transmitted field $U_1(x) = e^{jk_x x} t_1(x)$ can be calculated as:

$$U_2(x, k_x) = F\left[e^{jk_x x} t_1(x) e^{j\frac{\pi x^2}{\lambda z}}\right]\Bigg|_{k_x = \frac{2\pi x}{\lambda z}} e^{j\frac{\pi x^2}{\lambda z}}. \tag{S1}$$

The relationship among diffraction fields corresponding to different incident plane waves can be expressed as,

$$U_2(x, k_x) = U_{20}(x - \lambda k_x z/2\pi) e^{j(k_x x - \lambda k_x^2 z/4\pi)}, \tag{S2}$$

where $U_{20}(x) = F\left[t_1(x) e^{j\frac{\pi x^2}{\lambda z}}\right]\Bigg|_{k_x = \frac{2\pi x}{\lambda z}} e^{j\frac{\pi x^2}{\lambda z}}$ is the diffraction field with normal incidence. The diffraction field is linearly translated with $k_x$. When analyzing the local phase gradient of $U_{20}$ with respect to $x$, we split this into two contributions: one arising from the Fourier transform component $F\left[t_1(x) e^{j\frac{\pi x^2}{\lambda z}}\right]\Bigg|_{k_x = \frac{2\pi x}{\lambda z}}$, and the other from the quadratic phase exponential $e^{j\pi x^2/(\lambda z)}$. The Fourier component directly inherits the aperture size constraints without real-space superoscillation on the image plane, implying range of $[-D/(2\lambda z), D/(2\lambda z)]$. Meanwhile, differentiation of the quadratic phase yields $x/(\lambda z)$. We directly subtract $x/(\lambda z)$ from the local phase gradient of $U_{20}$ to find the simplified range $\left|\frac{1}{2\pi}\mathrm{Im}\frac{\partial \log U_{20}}{\partial x} - x/\lambda z\right| \le D/2\lambda z$. The change rate of the output field $U_2(x, k_x)$ with respect to $k_x$ can be calculated as,

$$\mathrm{Im}\frac{\partial \log U_2}{\partial k_x} = -\frac{\lambda z}{2\pi}\mathrm{Im}\frac{\partial \log U_{20}}{\partial x}\Big|_{x=\xi} + \xi, \quad \text{with} \quad \xi = x - \frac{\lambda k_x z}{2\pi}. \tag{S3}$$

Employing the prior derived bound, we have $\mathrm{Im}\frac{\partial \log U_2}{\partial k_x} \in \left[-\frac{D}{2}, \frac{D}{2}\right]$. Therefore, the change rate of the output field is limited by the aperture size. If another local element with an angle-independent transmittance profile $t_2(x)$ is added to the diffraction plane to form a doublet, the output field after the second modulation element is $U_3(x, k_x) = U_2(x, k_x)t_2(x)$. However, it doesn't change the change rate because the transmitted field at any spatial point depends only on the modulation and the incident field at the same point. Therefore, a single local element or a doublet cannot achieve superoscillatory superresolution imaging without real-space superoscillation due to the lack of angular sensitivity. In addition, if the numerical aperture (NA) is increased to deviate from the Fresnel approximation, there will be a degradation of angular resolution at large NA. In other words, a local lens with angular magnification could enhance the degraded angular resolution of high-NA imaging systems, yet the lack of angle-dependent response prevents it from achieving superresolution imaging via *k*-space superoscillation.

To further clarify the distinction of our method from existing angular magnification approaches, we provide a comparative analysis with the method reported in Ref. [25] from the main text. Both studies aim at enhancing resolution, yet differ fundamentally in terms of mechanisms, device architectures, and achieved performance standards.

Our work realizes far-field superresolution through *k*-space superoscillation enabled by a nonlocal, volumetric metalens with an angle-dependent transmission. Superresolution in our configuration arises from the extended local change rates of the transmitted field distribution exceeding the physical aperture's limit within a defined angular field of view (FOV). This mechanism inherently requires nonlocal coupling that depends explicitly on the incident angle.

In contrast, Ref. [25] primarily utilizes local metasurfaces designed to enhance angular resolution via PSF engineering. Specifically, under an NA of 0.97, Ref. [25] achieved an

angular resolution of 0.255°, surpassing the degraded angular resolution limit of 0.6005° but remaining inferior to the aperture-limited angular resolution of 0.1456°, achieving only 0.57 times this fundamental limit. The primary role of the designed single lens in Ref. [25] is to suppress aberrations at high NA, rather than explicitly surpassing the aperture-limited resolution. Additionally, the small-NA doublet configuration in Ref. [25] resolves three horizontal lines spaced by 0.0704°, compared to the hyperbolic phase profile lens benchmark resolving spacing of 0.084°, achieving a superresolution ratio (SR) of 1.19. This relatively low SR does not surpass the superoscillation criterion [2, 3] and thus generates no sidebands, indicating resolution enhancement through PSF engineering. This aligns with our earlier theoretical demonstration that a single local element or a doublet cannot achieve *k*-space superoscillation.

Consequently, the two works differ fundamentally in realization methods, physical principles, and performance outcomes. Ref. [25] employs local metasurfaces to achieve angular magnification through PSF engineering without extending the incoherent cutoff frequency beyond the aperture. In contrast, our study utilizes a nonlocal volumetric metalens to implement *k*-space superoscillation, extending the incoherent cutoff frequency beyond the aperture limit, thereby achieving superresolution imaging without image-plane sidebands within the designed FOV.

Moreover, multilayer metalenses have been designed to replace the bulky lens group for aberration-free imaging by increasing the angular magnification [4], yet the image resolution limited by the input aperture was not improved. For an ideal optical system without aberration, the numerical aperture decreases as the angle is stretched due to the conservation of optical etendue. This resulted in a compression of the lens-to-sensor distance with a constant resolution. The optimization of the angle-dependent PSF in the *k*-space superoscillation is similar to the optimization of the superoscillatory PSF in the real-space superoscillation, which requires a

comprehensive consideration of the Strehl ratio, spot size and sidelobe intensity [5-7].

## 3 Phase space representation of superoscillation

To further explain the concept underlying Fig. 1g and Fig. 1h, we provide their mathematical formulations. Figure 1g illustrates the Wigner distribution of the coherent field on the image plane, defined as,

$$W_{\mathrm{U}}(x_{\mathrm{i}}, k_{x_{\mathrm{i}}}) = \int_{-\infty}^{\infty} U(x_{\mathrm{i}} + \frac{x_{\mathrm{i}}'}{2}) U^{*}(x_{\mathrm{i}} - \frac{x_{\mathrm{i}}'}{2}) e^{-j k_{x_{\mathrm{i}}} x_{\mathrm{i}}'} dx_{\mathrm{i}}', \tag{S4}$$

where $U(x_{\mathrm{i}})$ represents the coherent PSF of real-space superoscillation on the image plane. Figure 1h corresponds to the aperture-plane view and is formulated by,

$$W_{\mathrm{U}}(x_{\mathrm{i}}, x, k_{\mathrm{x}}) = \frac{1}{2\pi} \int_{-\infty}^{\infty} U_{\mathrm{x_i}}(k_{\mathrm{x}} + \frac{k_{\mathrm{x}}'}{2})\, U_{\mathrm{x_i}}^{*}(k_{\mathrm{x}} - \frac{k_{\mathrm{x}}'}{2}) e^{j k_{\mathrm{x}}' x} \mathrm{d}k_{\mathrm{x}}', \tag{S5}$$

where $U_{x_{\mathrm{i}}}(k_{\mathrm{x}})$ denotes the angle-dependent complex amplitude of the transmitted field at the image plane at position $x_{\mathrm{i}}$, for an incident plane-wave transverse wavenumber $k_{\mathrm{x}}$, and $x$ is the input aperture coordinate reciprocal to $k_{\mathrm{x}}$. Note that Fig. 1h corresponds specifically to $x_{\mathrm{i}} = 0$. From this perspective, Fig. 1h visually represents how our engineered nonlocal response creates rapid variation with respect to $k_{\mathrm{x}}$ specifically within the FOV via weak measurement, enabling effective aperture expansion.

It is important to clarify that the regions with large amplitudes depicted in Fig. 1h do not represent energy contributions appearing on the image plane within the FOV. Rather, these bright parts illustrate the angle-dependent response of the nonlocal metalens to transverse wavenumbers $k_{\mathrm{x}}$ corresponding to incident angles outside the bounded FOV. Specifically, the higher amplitude transmission outside the FOV relative to that within the FOV is intrinsic to the weak-measurement basis of $k$-space superoscillation. In practical operation, the imaging is limited to objects within the bounded FOV, so the responses to objects outside the FOV, regardless of their relative amplitude, remain unexcited and do not contribute to the image formation process. Consequently, no additional blocking mechanisms are required beyond

ensuring the objects remain within the FOV. This property aligns with the fundamental principle that, unlike real-space superoscillation, *k*-space superoscillation does not produce unwanted image-plane sidebands.

To provide a direct comparison with Fig. 1g, we present a corresponding phase-space representation at the image plane for the *k*-space superoscillation system. Specifically, for each incident transverse wavenumber $k_x$, we calculate the complex field amplitude distribution $U(k_x, x_i)$ at the image plane and compute its Wigner distribution as defined by,

$$W_U(k_x, x_i, \xi) = \int_{-\infty}^{\infty} U(k_x, x_i + \frac{\tau}{2}) U^*(k_x, x_i - \frac{\tau}{2}) e^{-j\xi\tau}\, d\tau, \quad \text{(S6)}$$

where $x_i$ denotes the image-plane coordinate, and $\xi$ represents the local wavenumber conjugate to $x_i$, analogous to the interpretation of $k_x$ used in Fig. 1g.

Figure S1 explicitly compares the diffraction-limited local lens (Fig. S1a), *k*-space superoscillatory nonlocal metalens (Fig. S1b), and a real-space superoscillatory lens (Fig. S1c). For the local lens, the phase-space density forms a vertically oriented distribution at a fixed position determined by $k_x$. The distribution's width along the *x*-direction decreases with increasing NA, while its height along the $\xi$-direction increases. Changing $k_x$ results only in a rigid translation along the *x*-axis, leaving the local wavenumber $\xi$ support unchanged (Fig. S1a). In the case of our *k*-space superoscillatory metalens, the distribution exhibits similar local wavenumber confinement and *x*-direction width, yet the position shifts twice as fast with variations in $k_x$ along the *x*-axis (Fig. S1b). This visually demonstrates the angular magnification enabling superresolution without generating sidebands at the image plane. Conversely, real-space superoscillation involves extending local wavenumber beyond the diffraction cutoff within a confined region, resulting in pronounced sidebands outside the region-of-interest (ROI) (Fig. S1c). These distinctions clarify the underlying advantage of our approach: superresolution is achieved via engineered nonlocal angular responses, effectively expanding the effective aperture without generating image-plane sidebands.

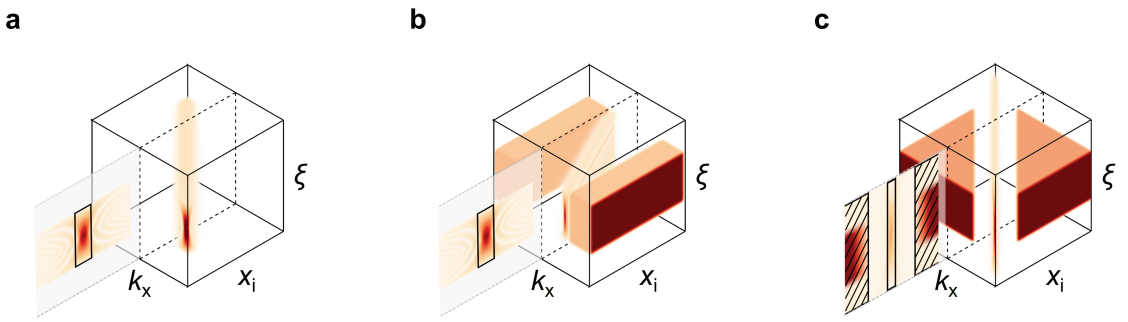



**Fig. S1 Phase-space representations at the image plane.** Wigner distributions $W_U(k_x, x_i, \xi)$ are shown for image-plane fields $U(k_x, x_i)$ corresponding to various incident transverse wavenumbers $k_x$. Coordinate $x_i$ denotes position on the image plane, and $\xi$ represents the conjugate local spatial frequency. **a** Diffraction-limited local lens: local wavenumber support is restricted by NA and the distribution's centroid simply shifts with changes in $k_x$. **b** *k*-space superoscillatory nonlocal metalens: local wavenumber support is restricted by NA, but the distribution's centroid moves twice as fast with $k_x$, clearly visualizing angular magnification and superresolution without generating sidebands at the image plane. **c** Real-space superoscillatory lens: local wavenumber support exceeds the NA-defined range, creating sub-diffraction features accompanied by substantial sidebands outside the ROI.

## 4 Weak measurement in *k*-space superoscillation

Due to the Fourier transform relation between $x$ and $k_x$, the normalized expectation [8] of the change rate of the transmitted field with respect to $k_x$ at any point $x'$ on the output plane is $\left|\frac{\langle T|\hat{x}|T\rangle}{\langle T|T\rangle}\right| = \left|\frac{\int_{-\infty}^{+\infty}|T(x',x)|^2 x dx}{\int_{-\infty}^{+\infty}|T(x',x)|^2 dx}\right| \leq \frac{D}{2}$, where $\langle\cdot|$ and $|\cdot\rangle$ are the quantum brackets and $\hat{x}$ represents the position operator. This reflects that the input aperture $D$ fundamentally limits the imaging system's resolution by limiting the Fourier spectrum of the transmitted field with respect to $k_x$. In addition to the above limitation on the overall resolution, to more accurately describe the resolution corresponding to different $k_x$, we define the local change rate [8] of the transmitted field as,

$$W(x', k_x) = \mathrm{Re}\frac{\langle k_x|\hat{x}|T\rangle}{\langle k_x|T\rangle}. \tag{S7}$$

The terms involved are explicitly defined via the angle-dependent transmitted field and transmission function as,

$$\langle k_x|T\rangle = \frac{1}{\sqrt{2\pi}}\, T(x', k_x), \tag{S8}$$

$$\langle k_x|\hat{x}|T\rangle = \frac{1}{\sqrt{2\pi}}\int_{-\infty}^{\infty} x\, e^{jk_x x}\, T(x', x)dx. \tag{S9}$$

Subsequently, using the momentum-space representation of the position operator, one obtains the relationship,

$$\frac{\langle k_x|\hat{x}|T\rangle}{\langle k_x|T\rangle} = -j\frac{\partial}{\partial k_x}\log T(x', k_x), \tag{S10}$$

which reveals that $W(x', k_x)$ can equivalently be represented by the phase gradient $\mathrm{Im}\frac{\partial \log T}{\partial k_x}$. Similar to the local spatial frequency in free space propagation approximating the direction of ray propagation [1], $W(x', k_x)$ approximates the position on the input plane affecting the $x'$ position on the output plane. As shown in Eq. (S7), the local change rate of the transmitted field $W(x', k_x)$ is a weak value with momentum post-selected, which can exceed far outside the normalized expectation of the change rate or the spectrum range of $T$ [9]. Because the measurement should be weak coupling, the amplitude of transmission $|\langle k_x|T\rangle|$ for $k_x$ within the bounded FOV should be reduced as a trade-off [10]. The reduced transmission amplitude is realized by strong interference of well-designed nonlocal response $T(x', x)$.

For a certain output position, such as $x_0' = -3D/8$, of a local 1D cylindrical lens, Fig. S2a shows the amplitude distribution of the transmission function $T(x_0', x)$, which corresponds to the cross-section of $T(x', x)$ indicated by the dashed line in Fig. S2b. Fig. S2c shows the real part of the angle-dependent transmitted field $T(x_0', k_x)$, which corresponds to the cross-section of $T(x', k_x)$ indicated by the dashed line in Fig. S2d. To clearly visualize the oscillatory behavior and account for the exponentially broad dynamic range of $|T(x_0', k_x)|$, we employ a logarithmic representation by plotting $\log|\mathrm{Re}\, T(x_0', k_x)|$. The oscillation frequency is directly

represented in the spacing between consecutive downward spikes, which is limited by the size of the input aperture $D$.

In comparison, Fig. S2e,f show a nonlocal metalens' amplitude distribution of the transmission function $T(x_0', x)$ at the same position $x_0'$. Fig. S2g shows the real part of the angle-dependent transmitted field $T(x_0', k_x)$, which corresponds to the cross-section of $T(x', k_x)$ indicated by the dashed line in Fig. S2h. Within the bounded FOV of the nonlocal metalens, the amplitude of the transmitted field is lower than that in the other region. The oscillation with respect to $k_x$ is faster than the limit imposed by the physical aperture size $D$. As analytically derived in Supplementary Section 1, for an incoherent imaging system, the cut-off frequency corresponds to the difference between the maximum and minimum change rate of the transmitted field on the lens output plane with respect to $k_x$. Therefore, the key to incoherent superresolution imaging is to have different change rates with respect to $k_x$ at different positions on the output plane, with the difference $\Delta W(k_x)_{max}$ between the maximum and minimum values exceeding $D$. In other words, because the weak measurement is localized at different spatial locations $x'$ and transverse wavenumbers $k_x$, the lens needs to exhibit an angle-dependent response at different spatial locations, necessitating nonlocality.

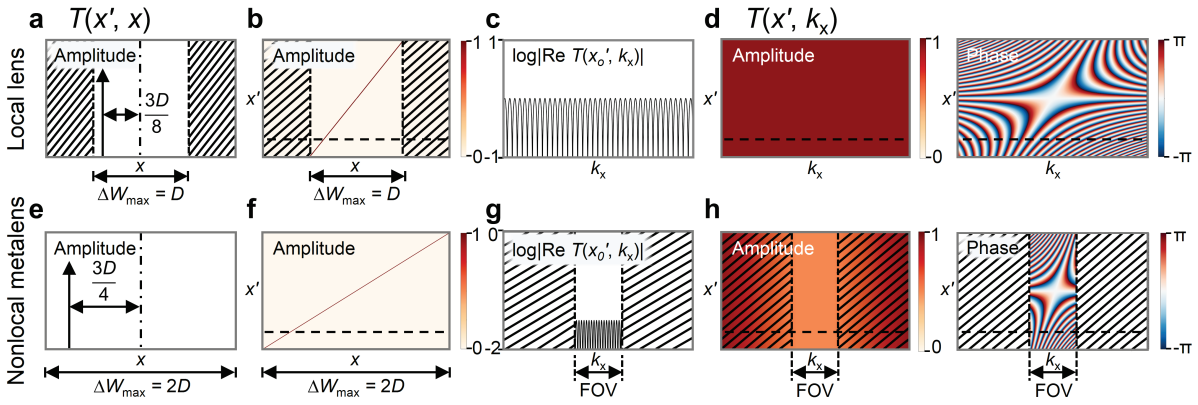



**Fig. S2 Weak measurement in *k*-space superoscillation. a** Amplitude distribution of the transmission function $T(x_0', x)$ at a certain output position $x_0' = -3D/8$ of a local 1D cylindrical lens. **b** Amplitude transmission function of a local 1D cylindrical lens. The dashed

line in Fig. S2b indicates the cross-section that corresponds to the line profile shown in panel **a**. **c** Angle-dependent transmitted field $T(x_0', k_x)$ at a certain output position $x_0' = -3D/8$ of a local 1D cylindrical lens. The absolute value of the real part is expressed as a logarithmic formation. **d** Complex amplitude angle-dependent transmitted field (left: amplitude, right: phase) of a local 1D cylindrical lens. The dashed line in Fig. S2d indicates the cross-section that corresponds to the line profile shown in panel **c**. **e** Amplitude distribution of the transmission function $T(x_0', x)$ at a certain output position $x_0' = -3D/8$ of a nonlocal metalens. **f** Amplitude transmission function of a nonlocal metalens. The dashed line indicates the cross-section that corresponds to the line profile shown in panel **e**. **g** Angle-dependent transmitted field $T(x_0', k_x)$ at a certain output position $x_0' = -3D/8$ of a nonlocal metalens. The absolute value of the real part is expressed as a logarithmic formation. **h** Complex amplitude angle-dependent transmitted field (left: amplitude, right: phase) of a nonlocal metalens. The dashed line indicates the cross-section that corresponds to the line profile shown in panel **g**. Note that the amplitude values do not correspond directly to those in panel **g** for clarity.

## 5 Comparison between real- and *k*-space superoscillation-based superresolution imaging

We compare the properties of real- and *k*-space superoscillation in Table S1. In both cases, the intensity at a certain point $x_i$ on the image plane is a superoscillation function $I(x_o, x_i)$ with respect to the position $x_0$ of the object point. To image an extended object with a range of $-x_{om}$ to $x_{om}$, the range of the image is $-Mx_{om}$ to $Mx_{om}$, where $M$ is the lateral magnification. For the edge A of the image $x_A = -Mx_{om}$, function $I$ should show superoscillation properties for $x_o \in [-x_{om}, x_{om}]$. The same applies to the opposite edge B of the image at $x_B = Mx_{om}$, where function $I$ should also exhibit superoscillation properties for $x_o \in [-x_{om}, x_{om}]$. Due to the spatially shift-invariant imaging property in real-space superoscillation, different positions on

the imaging plane have shifted response to the object position as shown in Fig. S3a, which can be expressed as $I(x_o, x_i) = I(x_o - x_i/M)$. Therefore, the region where the superoscillation occurs, namely the optimized ROI, should cover $-2x_{om}$ to $2x_{om}$ while the FOV is $2x_{om}$ [11].

**Table S1 Comparison between real- and *k*-space superoscillation**

| | Real-space superoscillation | *k*-space superoscillation |
|---|---|---|
| Superoscillation function | PSF with respect to $x$ | Transmission function with respect to $k_x$ |
| Weak value | Local spatial frequency | Local change rate of the transmitted field |
| Band limit of Fourier spectrum | Numerical aperture $2NA/\lambda$ | Aperture size $D$ |
| Imaging properties | Spatially shift-invariant imaging with local elements | Spatially shift-variant imaging with nonlocal elements |
| Sideband on the imaging plane | Present | Absent |
| Relationship between ROI and FOV* | $\mu(\mathrm{ROI}) = 2^N \times \mu(\mathrm{FOV})$ | $\mu(\mathrm{ROI}) = \mu(\mathrm{FOV})$ |
| Energy efficiency | $\frac{\int_{x\in \mathrm{ROI}} \mathrm{PSF}(x)dx}{\int_{-\infty}^{+\infty} \mathrm{PSF}(x)dx}$ | $\frac{\lvert T_0\rvert^2}{\max\lvert T(k_x)\rvert^2}$ |
| Expansion of the space-bandwidth product | Along the momentum dimension in the image plane | Along the spatial dimension in the aperture plane |

*$\mu$ represents measure in $N$-dimensional space

To image an extended object, such as a letter “E”, the ROI should be twice as wide as the FOV to prevent the imaging of point A on the one side being overwhelmed by the sideband of point B on the other side. Contrary to the real-space superoscillation, *k*-space superoscillation enables a spatially shift-variant response function $I(x_o, x_i)$. Therefore, its FOV can be the same as the ROI as shown as Fig. S3c, which cannot be achieved by modulation only in real- or *k*-space. While the range where superoscillation occurs is the same for each output field position, the specific superoscillatory functions are different. Note, however, that the FOV of superoscillation is inherently smaller compared to a conventional lens with identical NA, due

to the angular constraints necessary to achieve superresolution.

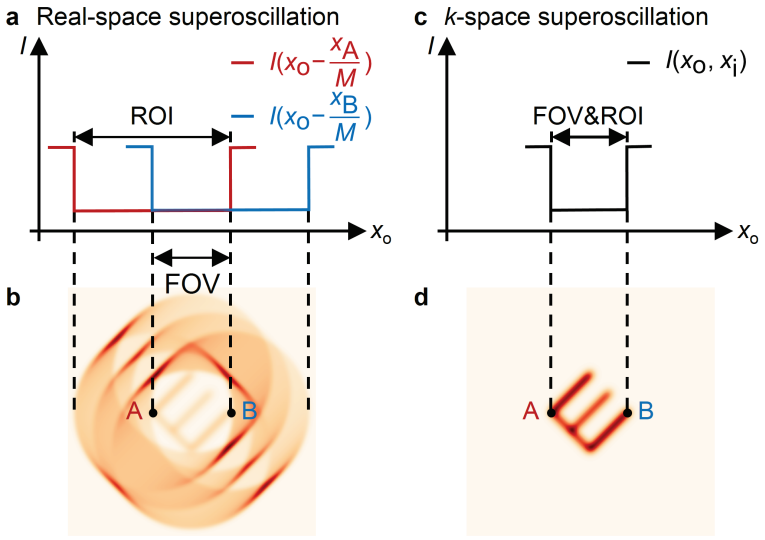



**Fig. S3 Comparison of ROI and FOV between real- and *k*-space superoscillation. a** Spatially shift-invariant intensity response $I(x_o - x_i/M)$ at a certain point $x_i$ on the image plane with respect to the position $x_0$ of the object point in real-space superoscillation. **b** Schematic diagram of the ROI's and FOV's size in extended object imaging of real-space superoscillation. **c** Spatially shift-variant intensity response $I(x_o, x_i)$ at a certain point $x_i$ on the image plane with respect to the position $x_0$ of the object point in *k*-space superoscillation. **d** Schematic diagram of the ROI's and FOV's size in extended object imaging of *k*-space superoscillation.

Moreover, the theoretical energy efficiency of *k*-space superoscillation, constrained by the fundamental limit of passive components, is determined by normalizing the transmission to the maximum value of 100%. In other words, any angle-dependent transmission distribution obtained through superoscillation design can theoretically be rescaled to attain this 100% transmission upper limit without violating physical constraints, as the relative complex amplitude relationships governing superoscillatory features remain preserved under linear scaling operations. There is no energy in the "sidelobes" outside the FOV. In contrast, the energy efficiency of the real-space superoscillation is the ratio of energy in the ROI to the PSF's total energy. To compare the real- and *k*-space superoscillation performance, we optimize the

nonlocal and local transmission functions in the same imaging condition with different hyper-parameters. The Pareto fronts [12] are fitted with these optimization results. As shown in Fig. S4, in the same condition, *k*-space superoscillation has a better performance in tradeoff among the FOV, energy efficiency and superresolution ability.

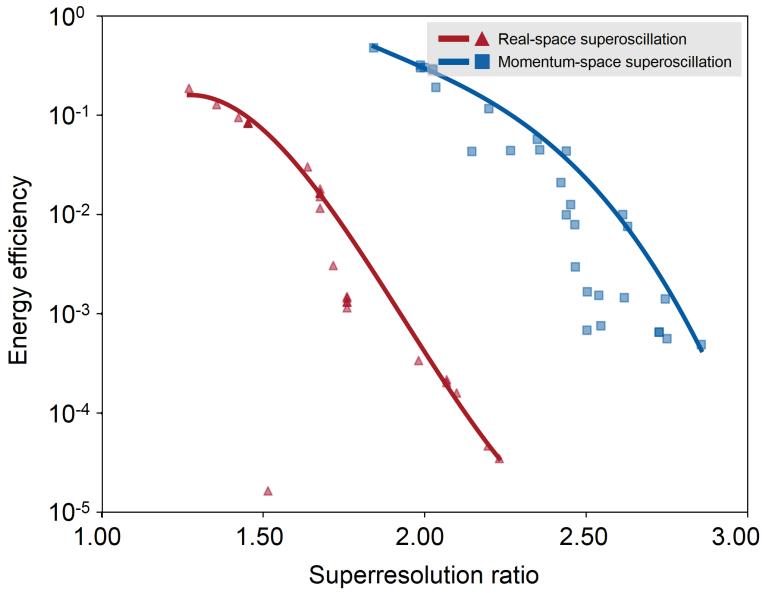



**Fig. S4 Comparison between the Pareto fronts of real-space and *k*-space superoscillation.** The curves represent the relationship between superresolution ratio and energy efficiency for real-space superoscillation (red) and *k*-space superoscillation (blue). Energy efficiency decreases exponentially with the superresolution ratio increasing linearly. The red triangles and blue squares correspond to optimization results of the real-space and *k*-space superoscillation, respectively.

Furthermore, real-space superoscillation is realized by sub-wavelength structures propagating to the far-field. Therefore, it is more sensitive to turbulence, dust and defocus during propagation compared to a converging spherical wave [13-15]. Fig. S5a,b shows the PSF formed by the propagation from the output plane of the imaging element to the image plane without any perturbation. It is important to note that the PSF for the *k*-space superoscillation (Fig. S5a) is diffraction-limited, consistent with its mechanism of achieving

superresolution via angular magnification rather than spot-size reduction. In contrast, the PSF for the real-space superoscillation (Fig. S5b) necessarily features a sub-diffraction hotspot required for its resolution enhancement. The real-space superoscillatory PSF is obtained by superimposing weight-optimized circular prolate spheroidal functions of the first five orders. The robustness to perturbations in free-space propagation is examined by placing five equally spaced random phase screens along the propagation path, with each screen imposing random phases with a standard deviation of 0.091 rad. Under the same conditions, the PSF in *k*-space superoscillation and the sidebands in real-space superoscillation are basically unaffected, but the vulnerable hot spot for the real-space superoscillation case is completely destroyed by the perturbation as shown in Fig. S5c,d.

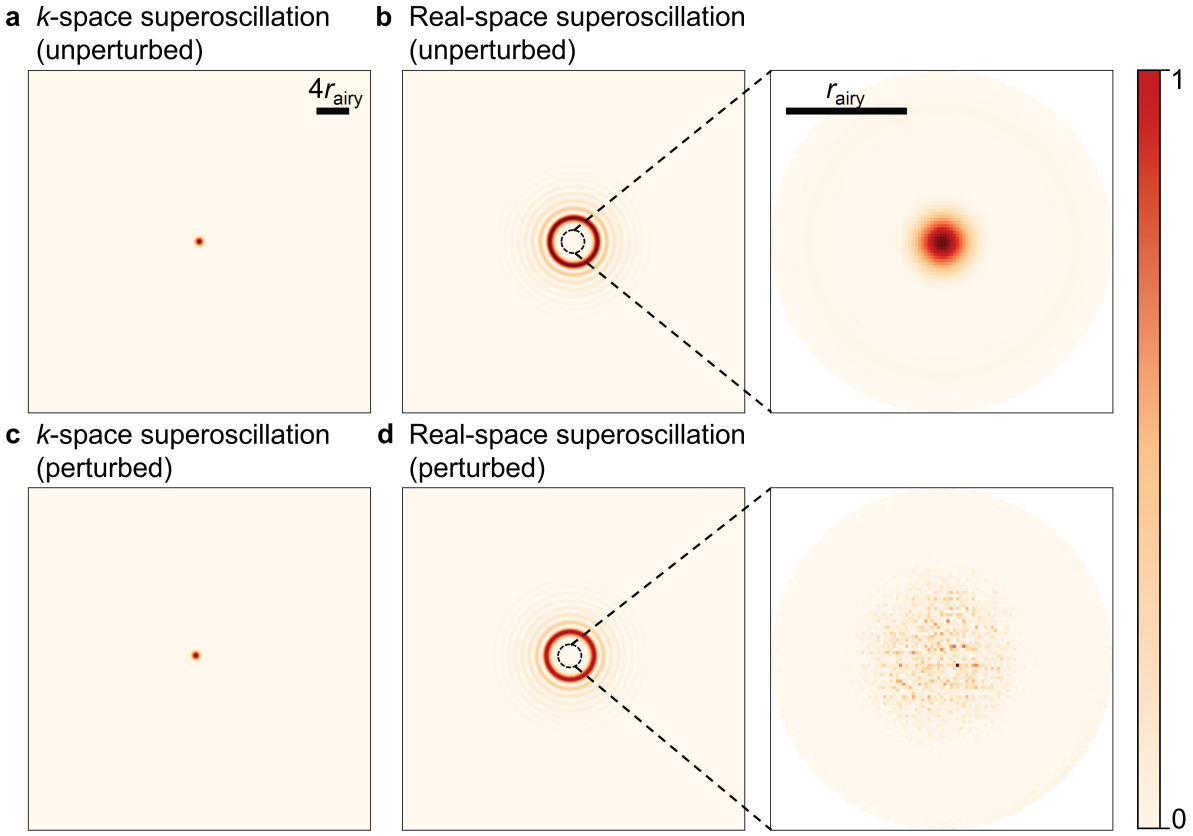



**Fig. S5 Comparison of robustness between real- and *k*-space superoscillation. a** PSF formed by the propagation from the output plane of the imaging element to the image plane without any perturbation in *k*-space superoscillation. **b** PSF formed by the propagation from

the output plane of the imaging element to the image plane without any perturbation in real-space superoscillation. The inset shows the zoom-in view of the hot spot within the sideband. **c** PSF perturbed by multiple random phase screens along the propagation path in *k*-space superoscillation. **d** PSF perturbed by multiple random phase screens along the propagation path in real-space superoscillation. The inset shows the perturbation destroys the hot spot within the sideband.

## 6 Derivation of target angle-dependent transmission profile for a 2D nonlocal metalens

When both the object distance $l_o$ and the image distance $l_i$ are finite, the angle-dependent transmitted field $T_s$ of the lens can be equivalently decomposed into $T_{s1}$ and $T_{s2}$ which transform a divergent spherical wave to a plane wave and transform the plane wave to a converging spherical wave, respectively, as,

$$T_{s1}(k_{x1}', k_{y1}', x, y) = \frac{1}{2\pi}\frac{l_o^3}{r_o}\left(\frac{1}{r_o} + \frac{j2\pi}{\lambda}\right)\frac{e^{\frac{j2\pi r_o}{\lambda}}}{r_o}, \tag{S11}$$

$$T_{s2}(x', y', k_{x1}, k_{y1}) = \frac{1}{2\pi}\frac{l_i^3}{r_i}\left(\frac{1}{r_i} + \frac{j2\pi}{\lambda}\right)\frac{e^{\frac{j2\pi r_i}{\lambda}}}{r_i}, \tag{S12}$$

$$r_o = \sqrt{\left(x + \frac{\lambda k_{x1}'}{\sqrt{4\pi^2 - \lambda^2 k_{x1}'^2}} l_o\right)^2 + \left(y + \frac{\lambda k_{y1}'}{\sqrt{4\pi^2 - \lambda^2 k_{y1}'^2}} l_o\right)^2 + l_o^2}, \tag{S13}$$

$$r_i = \sqrt{\left(x' - \frac{2\lambda k_{x1}}{\sqrt{4\pi^2 - \lambda^2 k_{x1}^2}} l_i\right)^2 + \left(y' - \frac{2\lambda k_{y1}}{\sqrt{4\pi^2 - \lambda^2 k_{y1}^2}} l_i\right)^2 + l_i^2}, \tag{S14}$$

where $(x, y)$, $(x', y')$ are the coordinate on the input and output plane, respectively. $(k_{x1}', k_{y1}')$, $(k_{x1}, k_{y1})$ are the intermediate variable corresponding the plane wave. Finally, the target angle-dependent transmission profile can be derived from the inverse Fourier transform of $T_{s1}$ and $T_{s2}$ as,

$$T_s(x', y', k_x, k_y) = \int_{-\infty}^{+\infty}\int_{-\infty}^{+\infty} F_{x,y}^{-1}\left[T_{s1}(k_x', k_y', x, y)\right] T_{s2}(x', y', k_x', k_y') dk_x' dk_y'. \tag{S15}$$

## 7 Electromagnetic calculations with MESTI

In this work, we have modified MESTI [16] to address specific requirements. Originally,

the spatial frequency interval between sampled propagation channels was determined as the reciprocal of the total lateral length, satisfying the Nyquist–Shannon sampling theorem. Here, for superresolution imaging, we increased the sampling density of the propagation channels to fully characterize the desired superresolution angular response. In the forward model, we consider *y*-polarized incident waves as specified in Fig. 2a. Given the *i*-th object point among all sampled *M* objects at ($x_i$, $y_i$) within the FOV, the incident wavefront is the corresponding spherical wave. Different incident wavefronts and their adjoint fields correspond to different input channels in the forward and adjoint simulation. Because an evanescent wave in free space does not transmit energy, we incorporated a normalization process by projecting the transmission fields onto all propagating output channels according to the Parseval theorem [1]. During the optimization process, MESTI calculates the response of 19 input channels simultaneously in a single run.

## 8 Details on the topology optimization procedure

The flow chart of the free-form topology optimization process is shown in Fig. S6a, with the minimization problem expressed as,

$$\underset{\varepsilon \in \{1,\, 2.25\}^N}{\operatorname{argmin}} \; L = -\sum_i w_i \ln(loss_{pi} + loss_{mi} + c), \tag{S16}$$

where $\varepsilon$ is the *N*-dimensional permittivity tensor, *i* is the objective point index, $w_i$ is the dynamic weight employed for the adaptive weighted method, and *c* is a constant ensuring non-negativity. The updated optimized variable is mapped to permittivity for connectivity and binarization using a graph-structured path planning algorithm and the tanh projection filter [17].

In this formulation, the first loss term, $loss_p$, quantifies the superresolution imaging capability by measuring the squared modulus of the cosine similarity between the target and the calculated angle-dependent transmission profiles. More specifically, for the *i*-th object point with an incident wavefront characterized by the angular spectrum $U_i(k_x, k_y)$, $loss_p$ is defined

as,

$$loss_{\mathrm{pi}}=\frac{\left|\int_{-\infty}^{+\infty}\int_{-\infty}^{+\infty}\left[\int_{-\infty}^{+\infty}\int_{-\infty}^{+\infty}T(x',y',k_{\mathrm{x}},k_{\mathrm{y}})U_{\mathrm{i}}(k_{\mathrm{x}},k_{\mathrm{y}})dk_{\mathrm{x}}dk_{\mathrm{y}}\int_{-\infty}^{+\infty}\int_{-\infty}^{+\infty}\tilde{T}_{\mathrm{s}}(x',y',k_{\mathrm{x}},k_{\mathrm{y}})\tilde{U}_{\mathrm{i}}(k_{\mathrm{x}},k_{\mathrm{y}})dk_{\mathrm{x}}dk_{\mathrm{y}}\right]dx'dy'\right|^2}{\left|\int_{-\infty}^{+\infty}\int_{-\infty}^{+\infty}T(x',y',k_{\mathrm{x}},k_{\mathrm{y}})U_{\mathrm{i}}(k_{\mathrm{x}},k_{\mathrm{y}})dk_{\mathrm{x}}dk_{\mathrm{y}}\right|^2\left|\int_{-\infty}^{+\infty}\int_{-\infty}^{+\infty}\tilde{T}_{\mathrm{s}}(x',y',k_{\mathrm{x}},k_{\mathrm{y}})\tilde{U}_{\mathrm{i}}(k_{\mathrm{x}},k_{\mathrm{y}})dk_{\mathrm{x}}dk_{\mathrm{y}}\right|^2},\quad \text{(S17)}$$

where the wavy line indicates complex conjugate. From another perspective, since $\int_{-\infty}^{+\infty}\int_{-\infty}^{+\infty}\tilde{T}_{\mathrm{s}}(x',y',k_{\mathrm{x}},k_{\mathrm{y}})\tilde{U}_{\mathrm{i}}(k_{\mathrm{x}},k_{\mathrm{y}})dk_{\mathrm{x}}dk_{\mathrm{y}}$ is the complex conjugate of the target focused phase profile, the above equation also equals the normalized intensity at the target peak position, thus constraining the peak displacement $\Delta r_{\mathrm{p}}$ of the focal spot from the optical axis.

The second loss term, $loss_{\mathrm{m}}$, is designed to control the size of the focal spot characterized by the distance between the two first minimums of the focal spot $\Delta r_{\mathrm{m}}$ to improve the imaging quality. For the *i*-th object point, $loss_{\mathrm{m}}$ is given by,

$$loss_{\mathrm{mi}}=\sum_{\mathrm{j}}\lambda_{\mathrm{ij}}\frac{\left|\int_{-\infty}^{+\infty}\int_{-\infty}^{+\infty}\left[\int_{-\infty}^{+\infty}\int_{-\infty}^{+\infty}T(x',y',k_{\mathrm{x}},k_{\mathrm{y}})U_{\mathrm{i}}(k_{\mathrm{x}},k_{\mathrm{y}})dk_{\mathrm{x}}dk_{\mathrm{y}}\int_{-\infty}^{+\infty}\int_{-\infty}^{+\infty}\tilde{T}_{\mathrm{s}}(x',y',k_{\mathrm{x}},k_{\mathrm{y}})\tilde{U}'_{\mathrm{ij}}(k_{\mathrm{x}},k_{\mathrm{y}})dk_{\mathrm{x}}dk_{\mathrm{y}}\right]dx'dy'\right|^2}{\left|\int_{-\infty}^{+\infty}\int_{-\infty}^{+\infty}T(x',y',k_{\mathrm{x}},k_{\mathrm{y}})U_{\mathrm{i}}(k_{\mathrm{x}},k_{\mathrm{y}})dk_{\mathrm{x}}dk_{\mathrm{y}}\right|^2\left|\int_{-\infty}^{+\infty}\int_{-\infty}^{+\infty}\tilde{T}_{\mathrm{s}}(x',y',k_{\mathrm{x}},k_{\mathrm{y}})\tilde{U}'_{\mathrm{ij}}(k_{\mathrm{x}},k_{\mathrm{y}})dk_{\mathrm{x}}dk_{\mathrm{y}}\right|^2}.\quad \text{(S18)}$$

where $U_{\mathrm{ij}}'(k_{\mathrm{x}},k_{\mathrm{y}})=U_{\mathrm{i}}(k_{\mathrm{x}},k_{\mathrm{y}})e^{j\frac{l_{\mathrm{o}}}{l_{\mathrm{i}}}(k_{\mathrm{x}}\Delta x(t_{\mathrm{j}})+k_{\mathrm{y}}\Delta y(t_{\mathrm{j}}))}$, $(\Delta x(t),\Delta y(t))$ represents a parametric curve consisting of first zero points around the target peak and the weights $\lambda_{\mathrm{ij}}$ for different object points and zero-point constraints are chosen such that points closer to the optical axis receive more emphasis. According to the Rayleigh criterion, two object points can just be resolved when the peak of one PSF coincides with the first minimum of the other PSF. The distance between the two object points, which is the resolution of the spatially shift-variant system, depends on the ratio of the lateral magnification characterized by the peak displacement $\Delta r_{\mathrm{p}}$ to the spot size characterized by the distance between the two first minimums $\Delta r_{\mathrm{m}}$. Therefore, $loss_{\mathrm{m}}$ and $loss_{\mathrm{p}}$ can effectively constrain the superresolution ability of the nonlocal metalens.

In the optimization process of *k*-space superoscillation, the field distribution changes rapidly and interferes delicately. The commonly used Method of Moving Asymptotes [18] may not be able to maintain a good approximation of the local convexity problem, which leads to instability in the optimization process. We choose the adaptive weighted method to ensure

similar performance for different object points. After several iterations, the weights corresponding to different objects are adjusted according to the corresponding loss function for negative feedback adjustment. The ln function also ensures the optimization results are relatively uniform within the FOV. In addition, the $N$-dimensional permittivity tensor is updated with a macropixel size of $2\Delta x = \lambda/6$, preserving the smallest manufacturable features, while simulations at a higher resolution ($\Delta x = \lambda/12$) are conducted to ensure computational precision.

Given the required symmetry in device response, we constrain the permittivity distribution through mirror symmetry, thereby reducing computational complexity by treating only one quadrant of the total pixel array as independent optimization parameters. To transition the continuous design variable $\eta$ to a binary variable. A tanh projection filter is applied according to the mapping relation $\frac{\tanh(0.5\beta) + \tanh(\beta(\eta - 0.5))}{2\tanh(0.5\beta)}$, with the parameter $\beta$ increased gradually each several iterations to enforce a sharper binary constraint. Furthermore, to ensure that each polypropylene sheet can be processed independently, we first use a breadth-first search algorithm to identify all connected regions. Next, we apply a greedy algorithm to generate a minimum spanning tree and process the regions that require reconnection using another breadth-first search. For the voxels needing adjustment, the relative permittivity is set symmetrically about the average value of air and polypropylene to guarantee connectivity. The entire optimization process requires approximately 18 hours using 1400 cores on Intel Xeon 6258R nodes in a high-performance computing system. Fig. S6b,c show the detailed relative permittivity profiles of each sheet.

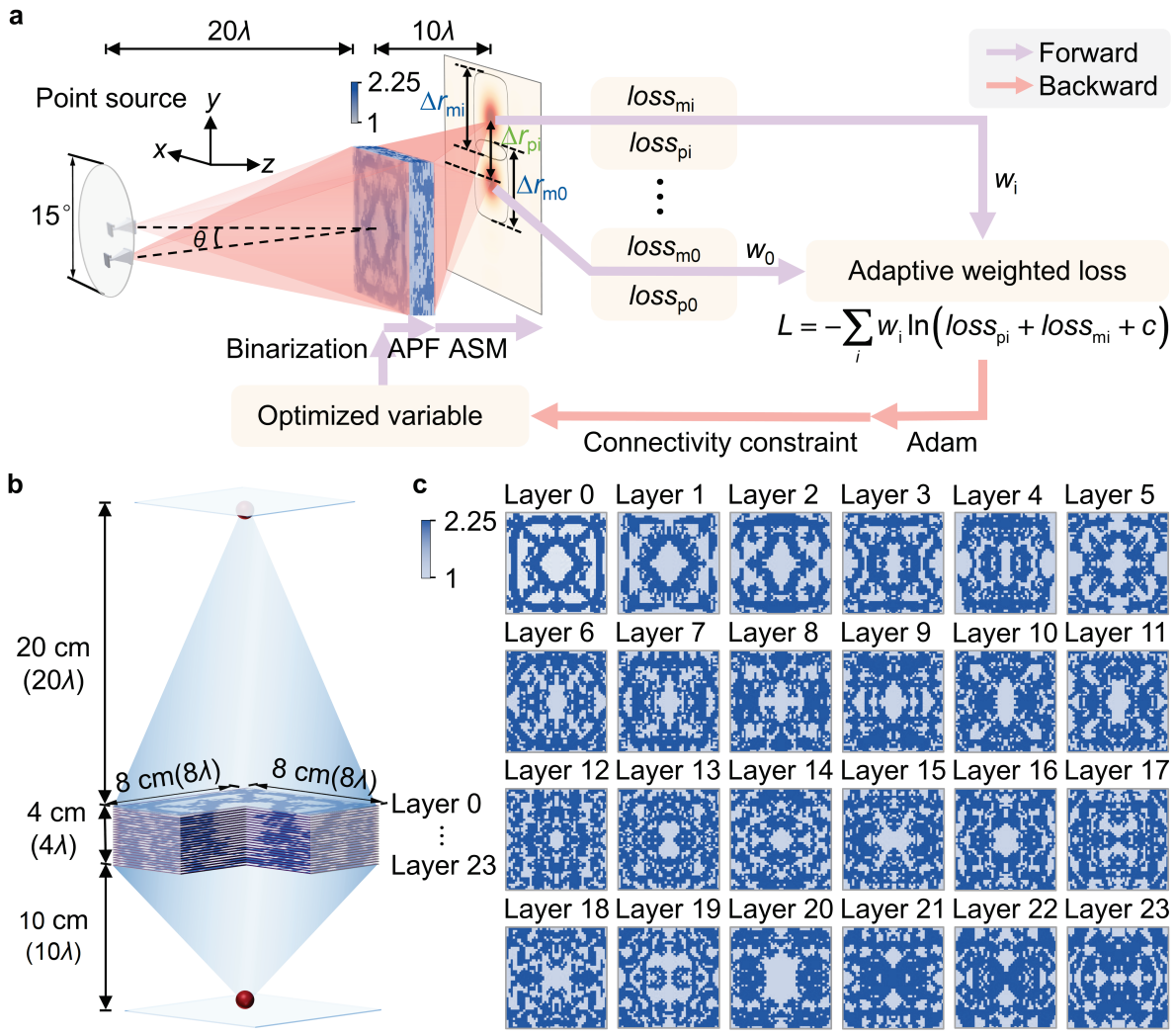



**Fig. S6 Topology optimization of the nonlocal metalens. a** Metalens optimization flow chart. The angle-dependent transmitted field and PSF for point sources within the bounded FOV of ± 7.5° are calculated using augmented partial factorization (APF) and angular spectrum method (ASM), resulting in a loss function $L$. $L$ is composed of two terms where $loss_p$ constrains the peak displacement of the focal spot from the optical axis $\Delta r_p$ and $loss_m$ constrains the distance between the two first minimums of the focal spot $\Delta r_m$. The gradient is obtained by the adjoint method. The optimization variable is updated by automatic differentiation with the adaptive moment estimation method (Adam) under the connectivity constraint and mapped to obtain the permittivity of the 3D metalens under the binarization requirement. **b** Schematic of geometry showing experimental configuration and order of each labeled layer. Areas with dark blue

colors are PP and areas with light blue colors are void. **c** Relative permittivity profiles of nonlocal metalens from main text.

## 9 Design of the local lens

The designed local lens used as a benchmark consists of two plano-convex polypropylene lenses with hyperbolic profile pasted together. The local lens has the same aperture size of 8 × 8 cm$^2$ (8 × 8$\lambda^2$). The hyperbolic height profile is expressed as,

$$h = \frac{\sqrt{z^2(n-1)^2 + 0.5 \times (n^2-1)D^2} - \sqrt{z^2(n-1)^2 + (n^2-1)r^2}}{n^2-1}. \quad \text{(S19)}$$

where the refractive index $n$ = 1.5, the aperture size $D$ = 8 cm (8$\lambda$) and $r$ is the distance from the optical axis. The profile towards the image side has $z$ = 10 cm (10$\lambda$) and the other profile toward the object side has $z$ = 20 cm (20$\lambda$).

## 10 Discrepancy between experiment and simulation

To construct an experimental setup that closely approximates the design and to minimize unwanted scattering, the metalens was surrounded by absorbing materials. We attribute the discrepancy between the measured and simulated PSF, particularly the observed sidelobes at the four corners and the distorted focal spot towards the periphery of the FOV, as shown in Fig. 3d, to the truncation of the diffracted wave by the absorbing materials. Specifically, since the metalens has a finite diffraction efficiency, the zero-order diffraction, in the form of a diverging spherical wave, can be truncated by the absorbing materials.

To test this hypothesis, we placed the horn antenna alone in the center of an empty channel. Fig. S7a depicts the diffraction field distribution on the image plane, which shows sidelobes at the four corners. We also used the wave-propagation method (WPM) [19] to calculate the diffraction field distribution with the object point located at the center and edge of the FOV, respectively, as shown in Fig. S7b,c. The above simulation results are consistent with the

experimental results. In addition, the simulation results show that compared to the center of the FOV, the focal spot corresponding to the edge of the FOV is truncated by the absorbing materials, as shown in Fig. S7d,e. The experimental result with $\theta = 7.50°$, as shown in Fig. 3b, is consistent with the above simulation results.

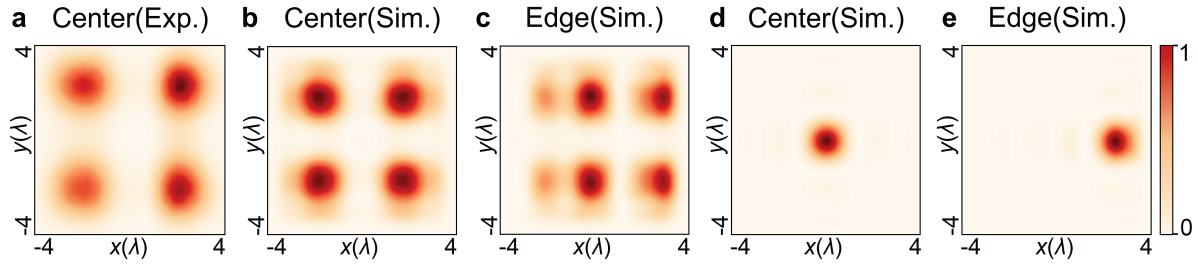



**Fig. S7 Diffraction field through an empty channel made of the absorbing material. a** Experimental intensity distribution when the horn antenna is located at the center of the FOV. **b-e** Intensity distribution simulated by the beam propagation method when **b** the object point is at the center of the FOV; **c** the object point is at the edge of the FOV; **d** the diffraction field's intensity distribution corresponding to the target phase distribution when the object point is located at the center of the FOV; **e** the diffraction field's intensity distribution corresponding to the target phase distribution when the object point is located at the edge of the FOV.

Under the experimental condition with surrounded absorbing materials, the captured PSF deviated in position and shape compared to the ideal PSF. However, since the distortion is linear, the superoscillation properties of spatially shift-variant PSFs remain unchanged. The dephasing effect [13] can be eliminated by PSF calibration and spatially-varying deconvolution. Fig. S8a,b plot the intensity at each peak position in Fig. 3c as a function of the object point's position for the local lens and nonlocal metalens, respectively. By tracking how the intensity at a single point on the image plane responds to shifts in the object's position, the resulting curve directly reflects the system's sensitivity to spatial displacements and indirectly characterizes its resolution [20]. By comparing the distance of two first minimums $\Delta r_{\mathrm{m}}$ of the nonlocal metalens to that of the local lens, SR ranging from 1.74 to 1.85 at the above several points can

be obtained across the entire FOV. At the edge of the FOV, the intensity minima of the local lens cannot be measured due to the limitations of the object's displacement range, at which point $\Delta r_{\mathrm{m}}$ was obtained by fitting the curve using a sinc square function.

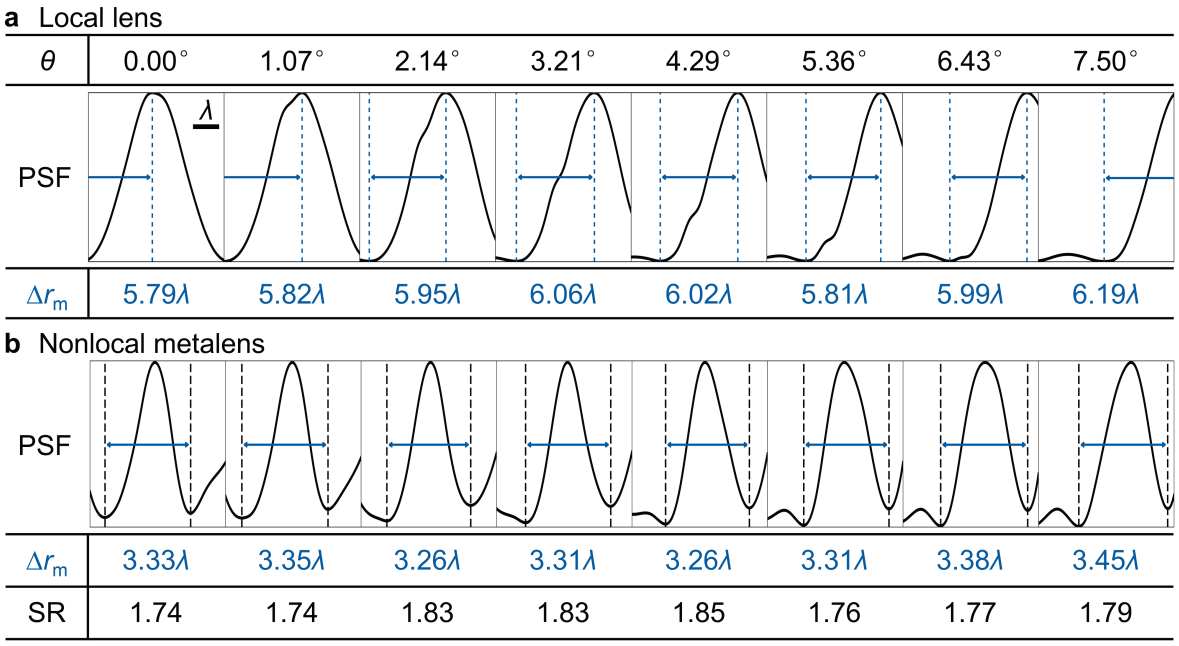



**Fig. S8 Variation of the intensity at different points on the image plane with respect to the object point's position. a** Measured intensity as a function of the object point's angular position at each peak position in Fig. 3c for the local lens. **b** Measured intensity as a function of the object point's angular position at each peak position in Fig. 3c for the nonlocal metalens.

The metalens was fabricated via a multi-step milling process with thickness tolerance on the order of tens of micrometers. The hole features exhibit similar precision. Besides, the finite cutter size leads to corner rounding. For assembly, alignment holes were machined around the edges, and the layers are tightly joined using polypropylene screws and nuts, yet misalignment between the layers remains the dominant error. To analyze the metalens' tolerance to assembly error, we simulated different lateral misalignment of the polypropylene sheets up to ±125% of the pixel size (± 2.09 mm). The average superresolution ratio as a function of the misalignment is shown in Fig. S9a. The error bars represent the varying range of superresolution ratios across

the FOV. The designed nonlocal metalens exhibits good tolerance with a slight resolution degradation for misalignments up to ±75% of the pixel size. Tolerances for machining and assembly errors could be improved by adding loss functions related to structural sensitivity.

We further clarify the energy distribution mechanism and the calculation of the simulated focusing efficiency mentioned in the main text. Our FDTD simulations indicate that 53.5% of the incident energy onto the nonlocal metalens is either reflected or scattered sideways. The sideways-scattered portion is absorbed by the perfectly matched layer (PML) in simulations or by the absorbing material in the experimental setup, and consequently does not influence the image plane distribution. The remaining 46.5% of the energy is transmitted. The mainlobe contains 11.37% of this transmitted power. When referenced against the power in the main lobe of the simulated local lens, this yields the final focusing efficiency of 6.53%. As shown in Fig. S9b, layer misalignment can result in a focusing efficiency lower than the designed value, which contributes the discrepancy between the simulated efficiency and the experimentally measured efficiency.

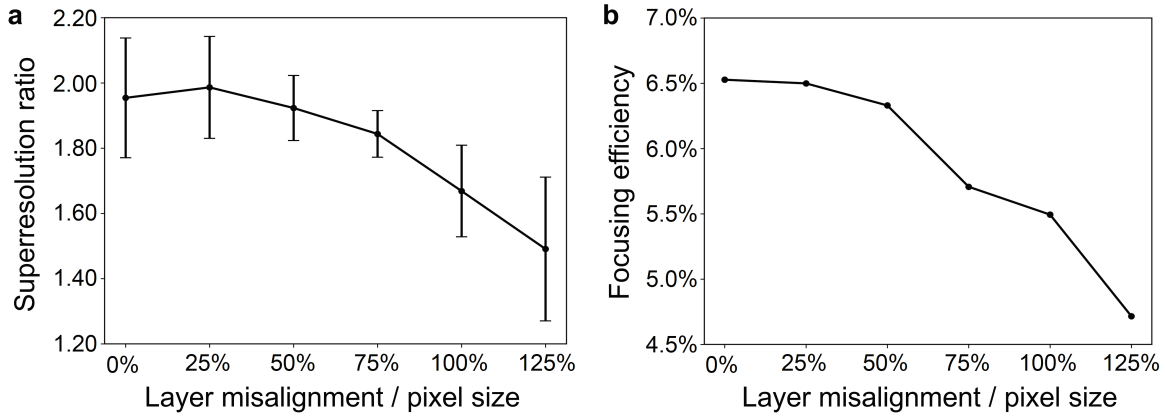



**Fig. S9 Metalens tolerance analysis for layer misalignment. a** Average superresolution ratio across the FOV as a function of layer misalignment. Layer misalignment is applied by alternating translations of the entire layer in the *x* and *y* direction. Error bars represent the varying range of superresolution ratios across the FOV. SR, superresolution ratio. **b** Focusing efficiency at the center of the FOV, defined as the ratio of the power in the main lobe to that of

the local lens, as a function of layer misalignment.

## 11 Comparative analysis of superoscillatory system

In superoscillatory imaging, efficiency, achieved SRs, and usable FOVs need to be considered simultaneously, since improving resolution or widening the FOV inherently leads to reduced efficiency. For clarity, Table S2 provides a detailed comparative analysis, listing the SRs, FOVs, and energy efficiencies reported in representative references. Specifically, the FOVs listed in the table are normalized by the Airy disk width, defined as the distance between its two first minima, enabling direct comparisons across different wavelengths and numerical aperture conditions.

**Table S2 Comparisons of the achieved SRs, FOVs, and efficiencies.**

| Method | Exp. /Sim. | Frequency domain | SR | FOV / Airy width | Efficiency |
|---|---|---|---|---|---|
| This work | Exp. | Microwave | ~2.00 | 1.03 | 2.24% |
| A. M. H. Wong et al., IEEE Trans. Antennas Propag. (2011) [21] | Exp. | | 1.33 | 0.50 | — |
| Z. Wu et al., Optical Materials (2022) [22] | Sim. | | 1.23 | — | — |
| J. Li et al., Frontiers in Materials (2022) [23] | Sim. | | 1.43 | — | 1.07% |
| C. Wang et al., Sci. Rep. (2015) [24] | Exp. | Optical | 2.00 | 0.48 | 0.10% |
| G. Yuan et al., Phys. Rev. Appl. (2019) [7] | Sim. | | 2.00 | 0.59 | 0.0036% |
| K. S. Rogers et al., Opt. Express (2018) [14] | Sim. | | 1.75 | 0.46 | 1.92% |
| D. Tang et al., Laser Photonics Rev. (2015) [25] | Exp. | | 1.47 | ~1.13 | 0.029% |
| G. H. Yuan et al., Light Sci. Appl. (2017) [26] | Exp. | | 1.04–1.33 | — | 0.56–3.5% |
| V. V. Kotlyar et al., Opt. Express (2017) [27] | Exp. | | 0.93–1.04 | — (on-axis spot only) | 2.98% |
| R. Zuo et al., Adv. Opt. Mater. (2018) [28] | Sim. | | 1.06–1.24 | 2.74 | 10.1% |
| K. S. Rogers et al., JPhys Photonics (2020) [29] | Sim. | | 1.71 | 0.41 | 8.2% |

For the referenced papers, the SRs, FOVs, and energy efficiencies values are extracted directly where available. When direct data are not explicitly provided, we indicate our calculation method below:

A. M. H. Wong et al. (2011) experimentally demonstrated superoscillatory focusing at 3 GHz. They achieved a focal spot size of 75% of the diffraction limit, corresponding to an SR of 1.33. The normalized FOV was 0.50. The focusing efficiency was not reported in this work.

Z. Wu et al. (2022) reported simulation results for a superoscillatory metalens operating at a wavelength of 2500 μm. They achieved a focal spot full-width-at-half-maximum (FWHM) of 0.418λ, compared to the diffraction limit of 0.513λ, yielding an SR of 1.23. The focusing efficiency was not reported. Because these SR values were below the superoscillation criterion [2, 3], their FOV was not limited by sidebands.

J. Li et al. (2022) reported simulation results for a superoscillatory lens operating at 11.1 GHz. They achieved a focal spot size of 0.7 times the diffraction limit, corresponding to an SR of 1.43. The effective efficiency was 1.07%, derived from the reported focusing efficiency of 0.9% normalized by the Airy disk main-lobe energy ratio of 83.78%. Because of the modest SR values, the FOV was not limited by sidebands.

For C. Wang et al. (2015), the reported SR ≈ 2.00 was calculated from the ratio between the distances of the first minimums of the Airy disk (82.8 μm) and the superoscillatory spot (41.4 μm). The reported ROI (79.35 μm) corresponded to approximately 0.96 times their Airy disk size, giving a normalized FOV of about 0.48. The efficiency of 0.10% was derived by multiplying the reported Strehl ratio (0.39%) by the squared spot-size ratio (0.51).

For G. Yuan et al. (2019), the reported FWHM was 0.28$\lambda$ for the superoscillatory spot and 0.56$\lambda$ for the Airy disk, yielding an SR of approximately 2.00. The ROI was 1.6$\lambda$, corresponding to a FOV equal 0.59 times the Airy disk diameter (1.36$\lambda$). Regarding efficiency, the authors reported that 0.003% of the total energy was contained within the region whose

radius is equal to the FWHM of the superoscillatory spot, compared to 83.05% for the Airy disk. Thus, the effective efficiency was approximately 0.0036%.

K. S. Rogers et al. (2018) numerically optimized a superoscillatory lens, achieving indicators including a SR of approximately 1.75 (based on the ratio of the FWHM of the superoscillatory spot to that of the Airy disk, 0.57), and a normalized FOV relative to the Airy disk's distance between the first minimums of approximately 0.46 (as their defined ROI radius equals 1.1 times the Airy disk's FWHM). Additionally, considering the reported ratio of peak intensities (Strehl ratio 0.059) and relative FWHM (0.57), we estimate their focusing efficiency as approximately 1.92%.

In D. Tang et al. (2015), the highest reported SR was approximately 1.47. From Fig. 7, the ROI was estimated as 7.1 μm, resulting in an FOV of about 3.6 μm. Given the Airy disk FWHM of 1.304 μm provided in the paper, this corresponded to an FOV approximately 1.13 times the distance between the first minimums of the Airy disk. The effective efficiency was approximately 0.029%, derived from the reported central spot efficiency of 0.024% normalized by the Airy disk main-lobe energy ratio of 83.78%.

G. H. Yuan et al. (2017) reported experimentally measured SR values ranging from 1.04 to 1.33, derived directly from the FWHMs of the superoscillatory spots and corresponding Airy disks. Because these SR values were below the superoscillation criterion [2, 3], their FOV was not limited by sidebands. The effective efficiencies ranged from approximately 0.56% to 3.5%, derived from the reported hotspot energy fractions of 0.47% to 2.9%, normalized by the Airy disk main-lobe energy ratio of 83.78%.

Kotlyar et al. (2017) reported near-field focusing at a distance of approximately 600 nm from the device surface, obtaining a focal spot with a FWHM ranging from 0.49$\lambda$ to 0.55$\lambda$, corresponding to the SR of 0.93–1.04 relative to the Airy spot (FWHM ~0.51$\lambda$). The effective efficiency was approximately 2.98%, derived from the reported focal-spot efficiency of about

2.5%, normalized by the Airy disk main-lobe energy ratio of 83.78%. Due to the consideration of only on-axis focusing without demonstrating imaging capability, the concept of FOV didn't apply to this work.

Zuo et al. (2018) reported a SR range of 1.06–1.24 based on their simulated focal spot FWHMs (0.42$\lambda$–0.49$\lambda$) relative to the Abbe diffraction limit (0.52$\lambda$). Due to the moderate SR, their angular FOV of 9° (2.74 times the angular Airy disk full width) was aberration-limited rather than sideband-constrained. Additionally, they calculated an efficiency of 10.1%, defined as the ratio of focused energy within a 10 μm × 10 μm area to the incident energy.

For K. S. Rogers et al. (2020), the reported SR of 1.71 is modest compared to the SR of ~2.00 achieved in our experiment. More critically, its reported FOV of 0.50$\lambda$ (corresponding to approximately 0.41 times the Airy disk diameter) is significantly smaller—by more than a factor of two—than the 1.03 Airy disk width FOV demonstrated in our work. The reported focusing efficiency is defined as the ratio of the energy contained within the superoscillatory region to the total energy of the function.

Taken together, these comparisons highlight that our experimental efficiency is over an order-of-magnitude higher than existing literature showing comparable SR and smaller FOV. While some numerical or experimental studies achieve higher efficiencies, they typically exhibit lower SR values, often below the superoscillation criterion [2, 3]. Consequently, our results represent a significant and practically relevant improvement in the trade-off among efficiency, resolution, and FOV.

Finally, to provide a comprehensive context, we further compare our approach with other representative categories of microwave superresolution techniques. Specifically, near-field microwave superresolution techniques [30, 31] rely on collecting evanescent waves, resulting in a limited working distance. For far-field applications, microwave superresolution techniques with model-based computational post-processing [32, 33] rely on specific scene assumptions

and face reliability concerns under complex conditions. As a more deterministic imaging modality, microwave superresolution techniques based on structured illumination [34, 35] hold significant potential but necessitate multiple illumination patterns and are restricted to a twofold resolution improvement by their underlying principles. In contrast, our *k*-space superoscillation approach offers the potential for further enhancement without the need for multiple illumination patterns and can be cascaded with existing modalities.

## 12 Spatially-varying deconvolution

The incoherent image formation model with a spatially-varying PSF can be given by,

$$I_{\mathrm{c}}(x_{\mathrm{i}}, y_{\mathrm{i}}) = \int_{-\infty}^{+\infty}\int_{-\infty}^{+\infty} I(x_{\mathrm{o}}, y_{\mathrm{o}})\mathrm{PSF}(x_{\mathrm{o}}, y_{\mathrm{o}}, x_{\mathrm{i}}, y_{\mathrm{i}})dx_{\mathrm{o}}dy_{\mathrm{o}}, \tag{S20}$$

where $I(x_{\mathrm{o}}, y_{\mathrm{o}})$ is the intensity of incoherent objects on the object plane, $I_{\mathrm{c}}(x_{\mathrm{i}}, y_{\mathrm{i}})$ is the captured image on the image plane, and $\mathrm{PSF}(x_{\mathrm{o}}, y_{\mathrm{o}}, x_{\mathrm{i}}, y_{\mathrm{i}})$ is the calibrated spatially-varying PSF for the object point at $(x_{\mathrm{o}}, y_{\mathrm{o}})$. The adaptive moment estimation method with auto gradient is used to solve the following loss function for spatially-varying deconvolution as,

$$\underset{I(x_{\mathrm{o}}, y_{\mathrm{o}})}{\mathrm{argmin}}\ loss = \left| I_{\mathrm{c}}(x_{\mathrm{i}}, y_{\mathrm{i}}) - \int_{-\infty}^{+\infty}\int_{-\infty}^{+\infty} \left| I(x_{\mathrm{o}}, y_{\mathrm{o}}) \right| \mathrm{PSF}(x_{\mathrm{o}}, y_{\mathrm{o}}, x_{\mathrm{i}}, y_{\mathrm{i}})dx_{\mathrm{o}}dy_{\mathrm{o}} \right|^2, \tag{S21}$$

where $I_{\mathrm{c}}(x_{\mathrm{i}}, y_{\mathrm{i}})$ is the superimposed image by measured PSFs with added 10 dB gaussian noise. The absolute values of $I(x_{\mathrm{o}}, y_{\mathrm{o}})$ after optimization are shown as the deconvolution result in Fig. 4d. The deconvolution approach described here does not incorporate additional regularization terms or rely on any prior datasets, distinguishing it fundamentally from deep learning-based reconstruction methods.

## 13 *k*-space superoscillatory imaging with higher superresolution ratio

The main obstacle to achieving higher resolution using a metalens with a specific permittivity distribution is the limited degrees of freedom and the requirement of permittivity binarization for realistic device fabrication. Without the constraint of binarization, the

optimization results can achieve higher resolution. As shown in Fig. S10, a metalens with a 50$\lambda$ aperture and a continuous permittivity profile achieved a superresolution ratio ranging from 2.09 to 2.65 across a FOV of up to 2.29°, representing an average 18% improvement over the results in Fig. 2 of the main text. From an effective medium perspective, achieving high-resolution subwavelength feature sizes that allow continuously adjustable permittivity (via changing fill fraction or duty cycle) can effectively enhance lens performance.

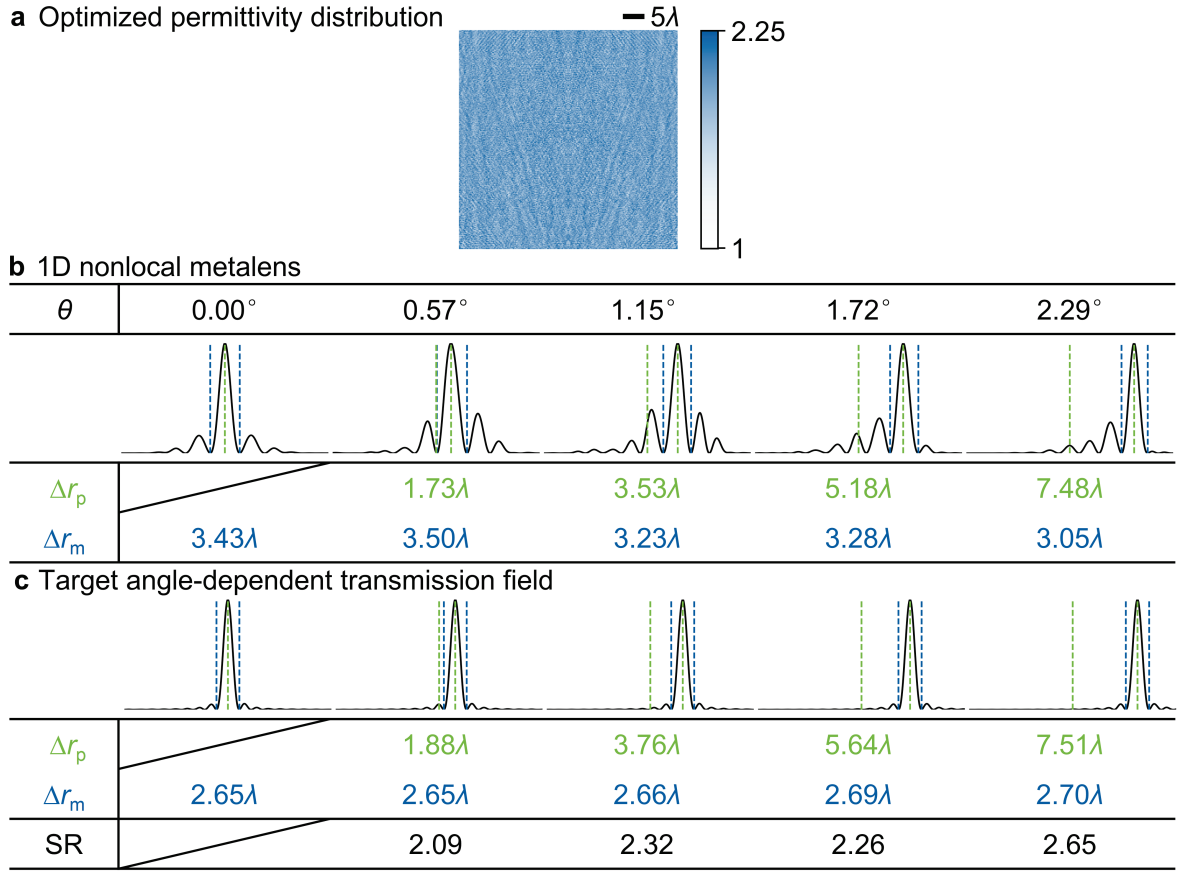



**Fig. S10 Design and optimization of 1D metalens with continuous permittivity profile. a** Optimized 1D metalens structure with the size of 50 × 50$\lambda^2$. **b** Simulated PSF as a function of the angular position of the point source calculated from the transmitted field using the angular spectrum method (ASM) for the optimized 1D nonlocal metalens. **c** Simulated PSF as a function of the angular position of the point source calculated from the transmitted field using

the ASM for the 1D ideal target response with triple lateral magnification of perfect imaging. SR, superresolution ratio.

As shown in Fig. 2c of the main text and Fig. S10b, the optimized PSFs do not perfectly match the target PSFs, and their differences manifest as background noise primarily arising from residual errors in the optimization process. Specifically, the finite number of layers, limited total thickness, and pixel resolution of nonlocal structures constrain the ability to realize the desired angle-dependent transmission perfectly, and thus increasing these design degrees of freedom can enhance the fidelity of the optimized response and reduce the residual background. To clearly illustrate how the device's degrees of freedom affect the observed background noise, additional optimizations were performed for varying total thicknesses. Consistent with expectations, increasing the total thickness suppressed the background noise, as shown in Fig. S11. For instance, the device optimized with 25$\lambda$ thickness (Fig. S11c) exhibited stronger background noise compared to the 50$\lambda$ case (Fig. S11b), and further decreasing thickness to 10$\lambda$ resulted in significant degradation of performance (Fig. S11d), clearly indicating that the main source of background noise is indeed the limited optimization capability associated with structural complexity.

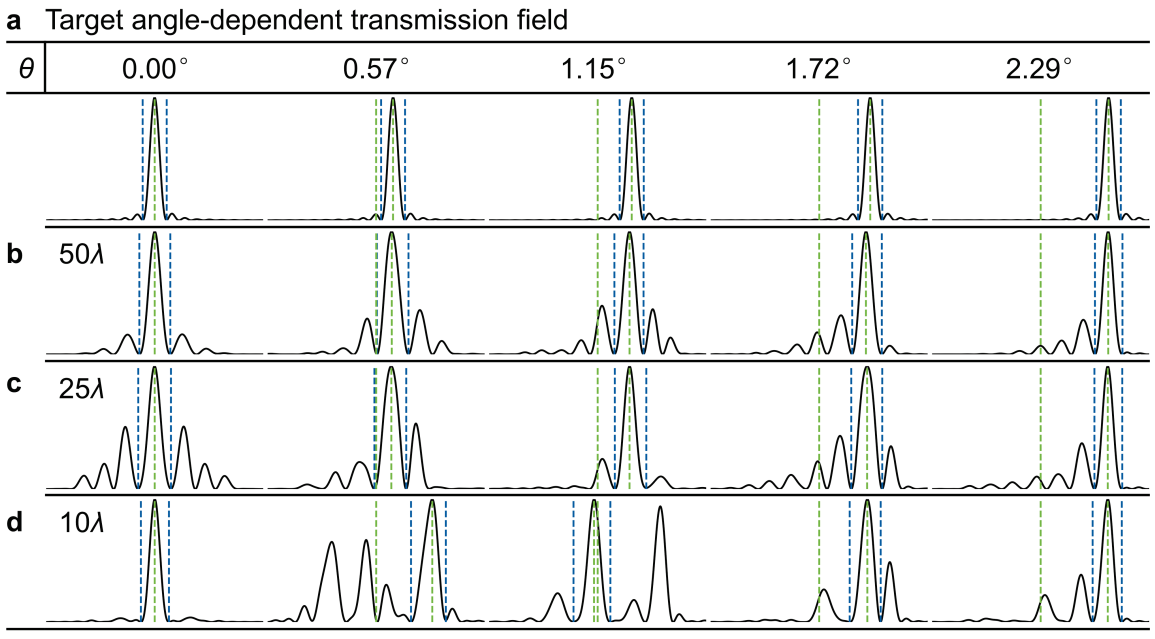


**Fig. S11. Influence of total structural thickness on the background noise of the 1D nonlocal metalens.** The black curves represent simulated PSFs, while the green dashed lines and blue dashed lines indicate the peak and central positions and the positions of the first minimums on either side of the peak, respectively. **a** Simulated PSF as a function of the 1D ideal target response with triple lateral magnification of perfect imaging. **b-d** PSFs correspond to devices optimized with total thicknesses of 50$\lambda$ (**b**), 25$\lambda$ (**c**), and 10$\lambda$ (**d**), respectively. PSFs are calculated via the angular spectrum method (ASM) as a function of incident angle across the designed FOV.

The observed reduction in background noise with increasing incident angles is due to the intrinsic principle of *k*-space superoscillation. Specifically, within the FOV, the focal spot energy is suppressed compared to regions outside the FOV to fulfill the weak measurement condition essential for *k*-space superoscillation. This suppression naturally leads to a gradient transition of energy distribution from inside to outside the FOV. At the boundary region of the FOV, the energy distribution experiences an intermediate state influenced by both the intentionally reduced energy inside the FOV and the higher energy levels outside it. Despite incorporating angularly dependent weighting during optimization to minimize such transitional effects, residual energy variations inevitably remain due to the finite degrees of freedom available in the design optimization process. On the other hand, the background noise, primarily originating from the limited modulation efficiency of the finite-thickness nonlocal metalens, remains relatively constant across varying angles. Consequently, as the incident angle increases, the relative intensity of the background noise diminishes due to the gradually enhanced focal spot energy levels near the FOV edges. This phenomenon manifests as a relative reduction in background noise with increasing angles.

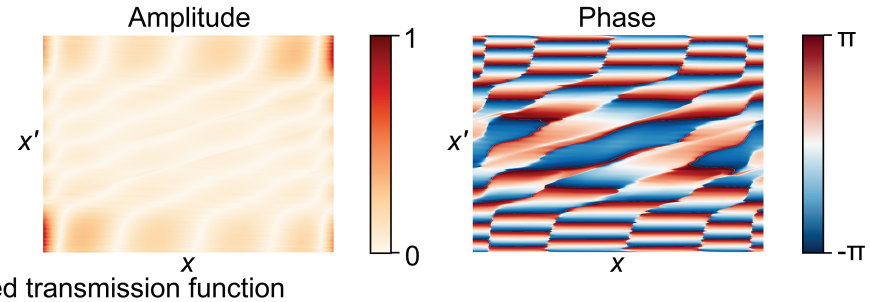
Furthermore, we designed the nonlocal response in a “theoretical manner” similar to designing a real-space superoscillation function [5, 36], which can obtain a larger design space.

Specifically, the optimized variable is no longer the permittivity distribution, but the transmission function $T(x', x)$ of a nonlocal optical element with a finite input aperture size. Because the angular spectrum propagation is differentiable, the adaptive moment estimation method with auto gradient is used to solve the following optimization problem expressed as,

$$\underset{T(x',x)}{\operatorname{argmin}} L = -\sum_{\mathrm{i}} w_{\mathrm{i}} \ln(loss_{\mathrm{pi}} + loss_{\mathrm{mi}} + c), \tag{S22}$$

where the symbols are 1D formation of those in Eq. (S16). The optimized complex transmission function is shown in Fig. S12a. Compared to the angle-dependent phase profile of a wide-angle metalens designed for perfect imaging without distortion [37, 38], the target angle-dependent transmission field retains the same numerical aperture while increasing the lateral magnification by three times, thereby achieving a threefold improvement in imaging resolution. The optimized nonlocal response achieved a resolution up to 2.7 times that of perfect imaging across the entire FOV of ± 1.5°, as shown in Fig. S12b,c.

**a** Optimized transmission function




**b** Optimized transmission function

| $\theta$ | 0.00° | 0.29° | 0.57° | 0.86° | 1.14° | 1.49° |
|---|---|---|---|---|---|---|
| PSF | | | | | | |
| $\Delta r_{\mathrm{p}}$ | | 0.58$\lambda$ | 1.23$\lambda$ | 1.87$\lambda$ | 2.60$\lambda$ | 3.10$\lambda$ |
| $\Delta r_{\mathrm{m}}$ | 2.56$\lambda$ | 2.60$\lambda$ | 2.60$\lambda$ | 2.55$\lambda$ | 2.55$\lambda$ | 2.40$\lambda$ |

**c** Target angle-dependent transmission field

| | | | | | | |
|---|---|---|---|---|---|---|
| PSF | | | | | | |
| $\Delta r_{\mathrm{p}}$ | | 0.69$\lambda$ | 1.38$\lambda$ | 2.07$\lambda$ | 2.75$\lambda$ | 3.58$\lambda$ |
| $\Delta r_{\mathrm{m}}$ | 2.44$\lambda$ | 2.44$\lambda$ | 2.44$\lambda$ | 2.44$\lambda$ | 2.45$\lambda$ | 2.46$\lambda$ |
| SR | | 2.37 | 2.51 | 2.59 | 2.73 | 2.66 |

**Fig. S12 Design and optimization of the transmission function and the angle-dependent transmitted field. a** Optimized complex transmission function (left: amplitude, right: phase). **b** Simulated PSF as a function of the angular position of the point source calculated from the optimized nonlocal response using the angular spectrum method (ASM). **c** Simulated PSF as a function of the angular position of the point source calculated from the transmitted field using the ASM for the 1D ideal target response with triple lateral magnification of perfect imaging. SR, superresolution ratio.

## 14 Cascaded *k*-space superoscillation superresolution imaging at optical frequencies

In many practical imaging systems, the achievable NA is inherently limited by multiple factors such as device footprint, fabrication constraints, working distance, available materials' refractive index bounds, and lens design geometry. Thus, under these realistic conditions where traditional imaging systems are fundamentally constrained to the diffraction-limited resolution determined by NA, demonstrating resolution beyond this limit is of practical significance.

We selected the NA used in this work to validate the concept while balancing practical engineering challenges. Increasing the NA inevitably leads to increased wavefront curvature. Consequently, designing an imaging device that focuses efficiently and corrects aberrations demands significantly greater three-dimensional design degrees of freedom, including increased nonlocal metalens thickness, higher pixel resolution per layer, and additional layers. These factors increase fabrication demands, including tighter dimensional tolerances and more precise interlayer alignment. Furthermore, higher NA metalens design substantially escalates computational complexity, requiring greater computing resources including larger memory, increased CPU/GPU core count, and longer runtime. In addition, microwave experiments inherently limit the illumination NA due to the finite divergence angle of the horn antenna used as a point source. Although it is technically feasible to increase the NA for designing a nonlocal metalens, doing so introduces significant engineering challenges rather than fundamental limits.

To circumvent the engineering challenges associated with higher-NA nonlocal element designs while achieving increased system NA, we propose a cascaded refractive-diffractive imaging configuration. In this hybrid architecture, a conventional high-NA microscope module consisting of an objective and a tube lens is placed before a nonlocal *k*-space superoscillation element. The high-NA objective collects a broad angular spectrum and corrects initial aberrations, forming an intermediate image with effective NA = 0.4 under image-side telecentric conditions. A thin field lens placed at this intermediate image relays the exit pupil onto the nonlocal element entrance pupil, ensuring proper pupil matching.

A practical optical implementation of the proposed cascaded imaging configuration is illustrated in Fig. S13a. An infinity-corrected microscope objective with NA = 0.95, followed by a tube lens, forms an intermediate image with an effective NA of 0.4 under image-side telecentric conditions. This intermediate image is located at the focal plane of the tube lens. A thin field lens placed precisely at this intermediate image plane relays the image with unity magnification, thereby ensuring accurate pupil matching between the exit pupil of the microscope module and the entrance pupil of the nonlocal element. For the nonlocal *k*-space superoscillation element, imaging a point formed at the intermediate plane is equivalent to imaging a point source positioned correspondingly. Consequently, the final sensor plane captures a superresolution image.

To theoretically validate the cascaded *k*-space superoscillation imaging principle, we derive the translationally-variant PSF for the entire cascaded system. After passing through the diffraction-limited relay, the field at the intermediate image plane is given by the coherent PSF $h_{\mathrm{DL}}(x_{\mathrm{r}})$, where $x_{\mathrm{r}}$ denotes coordinates in the intermediate image plane. The resulting field distribution $U_{\mathrm{i}}$ at the final image plane coordinates $x_{\mathrm{i}}$ following propagation through the field lens and the nonlocal element, characterized by a coherent translationally-variant PSF $h_{\mathrm{kSO}}(x_{\mathrm{r}}, x_{\mathrm{i}})$, is expressed as,

$$U_{\mathrm{i}}(x_{\mathrm{i}}) = \int h_{\mathrm{DL}}(x_{\mathrm{r}}) h_{\mathrm{kSO}}(x_{\mathrm{r}}, x_{\mathrm{i}}) dx_{\mathrm{r}}. \tag{S23}$$

Under the Fresnel approximation, accounting for the quadratic phase imparted by the thin field lens, the PSF $h_{\mathrm{kSO}}(x_{\mathrm{r}}, x_{\mathrm{i}})$ linking the intermediate image plane to the final image plane through the nonlocal element with transmission function $T(x, x')$ is,

$$h_{\mathrm{kSO}}(x_{\mathrm{r}}, x_{\mathrm{i}}) = \int_{-D/2}^{D/2} e^{j\frac{\pi(x' - x_{\mathrm{i}})^2}{\lambda r_{\mathrm{i}}}} \left[ \int_{-D/2}^{D/2} e^{j\frac{\pi(x - x_{\mathrm{r}})^2}{\lambda r_{\mathrm{o}}}} e^{-j\frac{\pi x_{\mathrm{r}}^2}{\lambda r_{\mathrm{o}}}} T(x, x')\, dx \right] dx', \tag{S24}$$

where $x$ and $x'$ represent coordinates on the input and output surfaces of the nonlocal element, and $r_{\mathrm{o}}$ and $r_{\mathrm{i}}$ denote the object distance and image distance of the nonlocal element, respectively.

To illustrate that the presence or absence of $h_{\mathrm{DL}}$ does not affect $k$-space superoscillation, we utilize the fact that the Fourier transform $F\{h_{\mathrm{kSO}}\}(k_{x_{\mathrm{r}}}, x_{\mathrm{i}})$ is inherently band-limited. Consequently, multiplication with the uniform Fourier transform of $h_{\mathrm{DL}}$ does not alter $h_{\mathrm{kSO}}$. Specifically, the Fourier transform of Eq. (S24) is given by,

$$H_{\mathrm{kSO}}(k_{x_{\mathrm{r}}}, x_{\mathrm{i}}) = \int_{-D/2}^{D/2} e^{j\frac{\pi(x' - x_{\mathrm{i}})^2}{\lambda r_{\mathrm{i}}}} \left[ \int_{-D/2}^{D/2} T(x, x') e^{j\frac{\pi x^2}{\lambda r_{\mathrm{o}}}} \left( \int_{-\infty}^{+\infty} e^{-jk_{x_{\mathrm{r}}} x_{\mathrm{r}}} e^{-j\frac{2\pi x x_{\mathrm{r}}}{\lambda r_{\mathrm{o}}}} dx_{\mathrm{r}} \right) dx \right] dx'. \tag{S25}$$

Because the inner integral $\int_{-\infty}^{+\infty} e^{-jk_{x_{\mathrm{r}}} x_{\mathrm{r}}} e^{-j\frac{2\pi x x_{\mathrm{r}}}{\lambda r_{\mathrm{o}}}} dx_{\mathrm{r}}$ reduces to a δ-function, enforcing $|k_{x_{\mathrm{r}}}| \leq \frac{\pi D}{\lambda r_{\mathrm{o}}} = k_{\max}$, $H_{\mathrm{kSO}}(k_{x_{\mathrm{r}}}, x_{\mathrm{i}}) \equiv F\{h_{\mathrm{kSO}}\}(k_{x_{\mathrm{r}}}, x_{\mathrm{i}})$ is band-limited to $|k_{x_{\mathrm{r}}}| \leq k_{\max}$. Since the relay's coherent transfer function, $F\{h_{\mathrm{DL}}\}(k_{x_{\mathrm{r}}}) = \mathrm{rect}(k_{x_{\mathrm{r}}}/2k_{\mathrm{DL}})$, has a unit amplitude within its passband and given the pupil matching condition ($k_{\max} = k_{\mathrm{DL}}$), we find that,

$$H_{\mathrm{DL}}(-k_{x_{\mathrm{r}}})\, H_{\mathrm{kSO}}(k_{x_{\mathrm{r}}}, x_{\mathrm{i}}) = H_{\mathrm{kSO}}(k_{x_{\mathrm{r}}}, x_{\mathrm{i}}). \tag{S26}$$

The diffraction-limited relay passes the superoscillation spectrum unchanged. Therefore, cascading a diffraction-limited relay does not alter or degrade the $k$-space superoscillation characteristics.

To address the engineering challenges associated with fabricating volumetric nonlocal metalenses at optical frequencies, we propose utilizing cascaded diffractive layers. This multilayer design leverages free-space propagation between cascaded diffractive phase-modulation layers to achieve nonlocal response, effectively balancing computational resources,

fabrication feasibility, and superresolution imaging performance. Experimental demonstrations of comparable cascaded diffractive layers have been reported, including three-layer and five-layer structures fabricated directly onto fiber tips by two-photon polymerization (TPP) using standard photoresists [39]. Specifically, these devices achieved pixel pitches of approximately 875 nm and inter-plane spacings around 35 μm, closely aligning with the design specifications necessary for our optical-frequency implementation. At optical wavelengths, precise interlayer alignment is typically achieved using established methods employing alignment marks [40], which enable sub-pixel alignment accuracy. Thus, cascaded diffractive layers offer a practically viable route for scaling our *k*-space superoscillation imaging approach to optical wavelengths.

Such miniaturized cascaded diffractive layers are suited for integrated applications, including fiber-optic endoscopy. Furthermore, they can be employed to construct arrays of nonlocal metalenses, enabling coverage of larger areas through FOV stitching [41]. Specifically, to extend the effective FOV in this configuration, the single field lens can be replaced with a field lens array [42]. The array parallelizes the strategy of scanning a field stop at the intermediate image plane to realize FOV stitching [24]. In this setup, the field lens array can couple different local regions of the intermediate image formed by the high-NA objective and tube lens into a corresponding array of nonlocal *k*-space superoscillation elements, thereby achieving FOV stitching. Beyond these miniaturized implementations, macroscopic [40] and CMOS-integrated [43, 44] cascaded diffractive layers have also been realized at optical wavelengths, demonstrating the scalability of these architectures.

Concerning the linewidth achievable with TPP, the laser wavelength employed for TPP fabrication can be shorter than the operational wavelength of the device, which facilitates relatively higher fabrication precision. Additionally, TPP relies on a nonlinear absorption process characterized by a distinct polymerization threshold effect. Curing occurs exclusively

within the minute volume at the center of the focal spot where the intensity exceeds this threshold. This phenomenon ensures that the effective voxel size is substantially smaller than the diffraction limit associated with linear (single-photon) exposure, thereby enabling the fabrication of the fine features [45-47].

Below, we further present an optimized four-layer design for cascaded imaging architectures at optical frequencies. Specifically, we have designed and optimized cascaded diffractive layers comprising a stack of four phase-modulation planes, each sampled on 140 × 140 pixels with a pitch of 875 nm. The separation between adjacent phase-modulation planes is 128.4 μm, and the system operates at a wavelength of 1550 nm. To mitigate the adverse effects caused by pixelated phase modulation, we place thin microlenses with focal lengths of 118.7 μm and -626.5 μm at the first and last phase-modulation planes, respectively. Additionally, a circular obscuration is introduced to block the central region of the first phase-modulation plane, as shown in Fig. S13b, to enhance *k*-space superoscillation performance under constraints of discrete pixelation and fabrication feasibility. For the *k*-space superoscillation element within the cascaded relay system, the object and image distances are set to 140.3 μm and 1000 μm, respectively, with a FOV of 4.90 μm. As depicted in Fig. S13a, a high-NA objective (NA = 0.95) coupled with a tube lens forms an intermediate image at an effective NA of 0.4 under image-side telecentric conditions. Subsequently, a thin field lens relays the pupil onto the Fourier plane, where the nonlocal *k*-space superoscillation element implementing the *k*-space superoscillation mapping is located, and the sensor captures the final image.

During the optimization, we employ a differentiable angular spectrum propagation model as the forward model and utilize the Adam optimizer to iteratively update the phase values at each pixel of each diffractive layer. The loss function is defined as the mean squared error between the intensity distributions of the simulated PSFs at different incidence angles and their

corresponding diffraction-limited PSFs with twice the lateral magnification.

Figure S13b illustrates the optimized phase distribution of the cascaded diffractive layers designed for the cascaded *k*-space superoscillation imaging system described above. To facilitate a direct evaluation, Fig. S13c provides the PSFs obtained in the cascaded diffractive layers optimized for a direct-imaging configuration. Figure S13d presents the PSFs for the cascaded configuration when the *k*-space superoscillation element is replaced with a conventional local lens. Figure S13e shows the PSFs corresponding to the cascaded configuration utilizing the *k*-space superoscillation cascaded diffractive layers, exhibiting quantitatively calculated SRs from 2.08 to 2.79. The minimal difference between Fig. S13c and Fig. S13e highlights the feasibility of cascaded *k*-space superoscillation configurations.

Figure S14 presents simulated superresolution imaging results comparing cascaded refractive-diffractive configurations with a conventional local lens and a nonlocal *k*-space superoscillation element. Figure S14a shows the target object, where the line spacing of the letter 'E' is set to half the diffraction limit. Simulated imaging results of the letter 'E', obtained using the cascaded local lens and the cascaded nonlocal *k*-space superoscillation element, are illustrated in Fig. S14b, c, respectively. The conventional imaging system cannot resolve the sub-diffraction-limit features of the letter 'E' (Fig. S14b), whereas the *k*-space superoscillation system effectively resolves these details (Fig. S14c), demonstrating approximately twofold superresolution under identical imaging conditions. Additionally, closely spaced slits, representing differential changes in object positions, further illustrate the resolution enhancement. Figure S14d shows the target object of double-slits with spacing set to half the diffraction limit. Corresponding simulated imaging results comparing the cascaded local lens and the nonlocal *k*-space superoscillation element are presented in Fig. S14e, f. These comparative results illustrate that the *k*-space superoscillation element increases the spacing between images of closely spaced slits by allowing the transmitted field's local rate of change,

with respect to the incident transverse wavenumber, to surpass the global limit imposed by the aperture size (represented by the local lens). Consequently, this effectively extends the system's resolution beyond the diffraction limit. Fig. S14g further illustrates this improvement through comparative MTF plots, clearly demonstrating the extended spatial-frequency response achieved by the *k*-space superoscillation element.

The required number of modulation layers is determined by the degrees of freedom necessary to achieve the desired nonlocal response for *k*-space superoscillation. A fully nonlocal response requires $N_{\mathrm{d}}^4$ degrees of freedom for diffraction layers discretized by $N_{\mathrm{d}} \times N_{\mathrm{d}}$ pixels at both input and output surfaces. Increasing the number of modulation layers inherently increases the achievable rank of the nonlocal response. This enhanced rank allows for a more accurate realization of the complex, angle-dependent transmission function required for *k*-space superoscillation. Consequently, while a relatively small number of layers—such as the four layers demonstrated in our simulation—is sufficient to provide the necessary nonlocal response to achieve *k*-space superoscillation, increasing the layer count generally allows for higher resolution at the same efficiency (or improved efficiency at the same resolution). We also note that the performance improvement tends to saturate as the number of layers increases, a phenomenon similar to observations in linear diffractive deep neural networks [39].

The choice of 24 layers for the microwave experiment was dictated by the balance between achieving the target superresolution performance and the physical constraints of the experimental setup. In multi-layer cascaded diffractive structures, the interlayer spacing must be sufficiently long to allow for adequate modulation of the diffraction field [48] and to achieve the necessary angular response, a requirement constrained by the pixel size and the free-space propagation kernel. While the required total thickness remains compact in the optical regime, these dimensions scale significantly in the microwave regime due to the longer wavelength. The resulting total device thickness and the lateral dimensions of the polypropylene boards

were challenging to accommodate and accurately characterize within the physical constraints of the available microwave anechoic chamber. To ensure performance, we chose to increase the number of layers within a reasonable and practically manageable volume.

Notably, a two-layer configuration is insufficient to achieve *k*-space superoscillation. Firstly, fewer modulation layers inherently limit the achievable rank of the nonlocal response, preventing accurate realization of the required transmission function for *k*-space superoscillation. Secondly, despite the presence of two phase-modulation planes, the first plane functions solely as an aperture diaphragm. Only the second plane can introduce energy loss and suppress the transmitted amplitude within the FOV to satisfy the weak measurement condition. Therefore, as analyzed in Supplementary Section 2, a two-layer structure can merely transfer real-space superoscillation from the image plane onto the second modulation plane. Consequently, this scenario remains fundamentally constrained by the same limitation as real-space superoscillation, requiring the ROI to be at least twice as wide as the FOV.

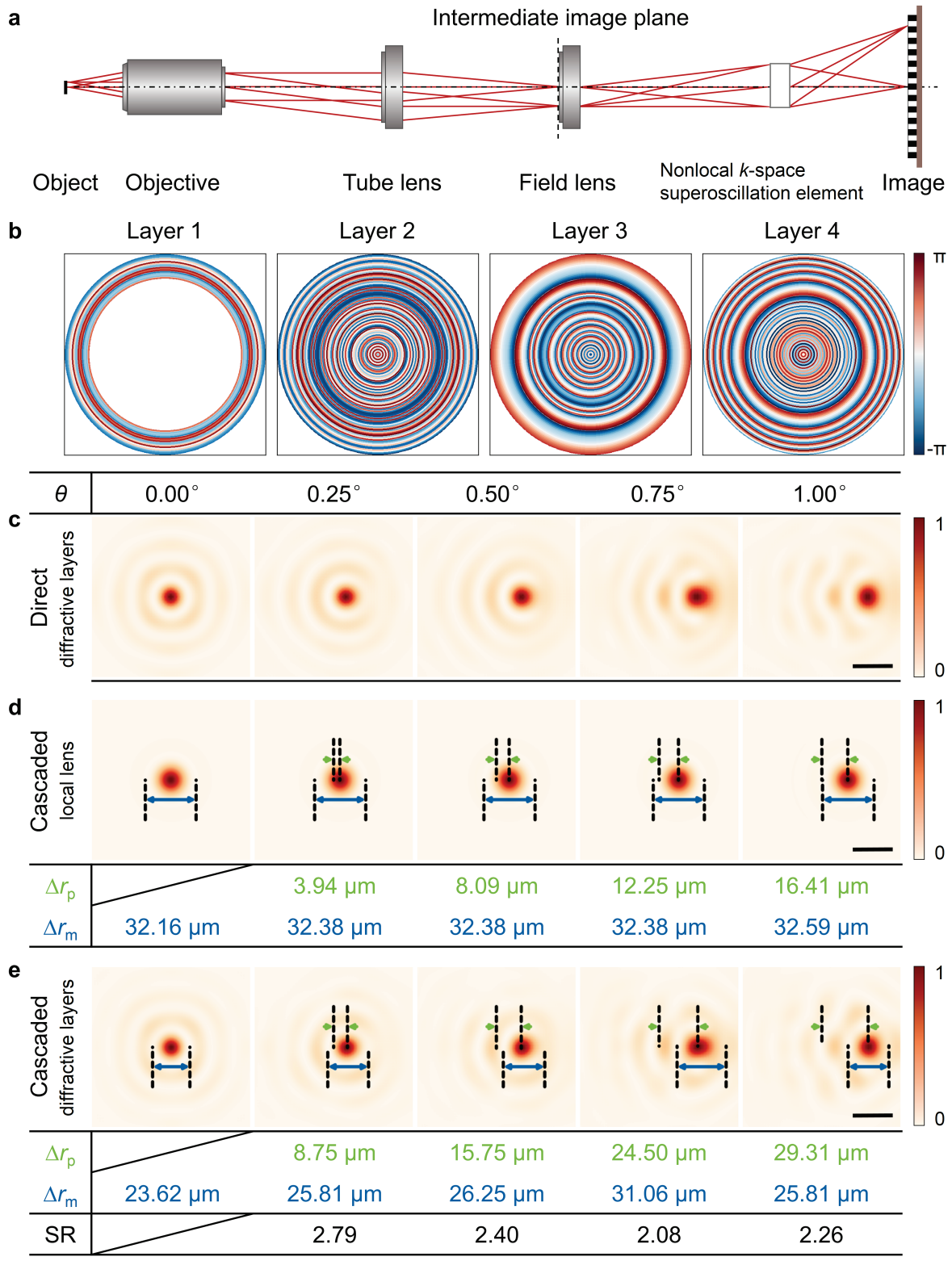



**Fig. S13 Cascaded refractive-diffractive imaging with *k*-space superoscillation. a** Schematic of the cascaded architecture: a high-NA objective (NA = 0.95) and tube lens form

an intermediate telecentric image at NA = 0.4. A thin field lens relays the pupil onto the nonlocal *k*-space superoscillation element, and the sensor records the final image. **b** Phase distribution of each layer in the cascaded diffractive layers designed for the cascaded *k*-space superoscillation imaging system. **c-e** PSFs of: **c** direct imaging with cascaded diffractive layers; **d** cascaded configuration with a conventional local lens at the same NA; **e** cascaded configuration with the *k*-space superoscillation cascaded diffractive layers. Scale bar: 25 μm. $\theta$ is the chief ray angle.

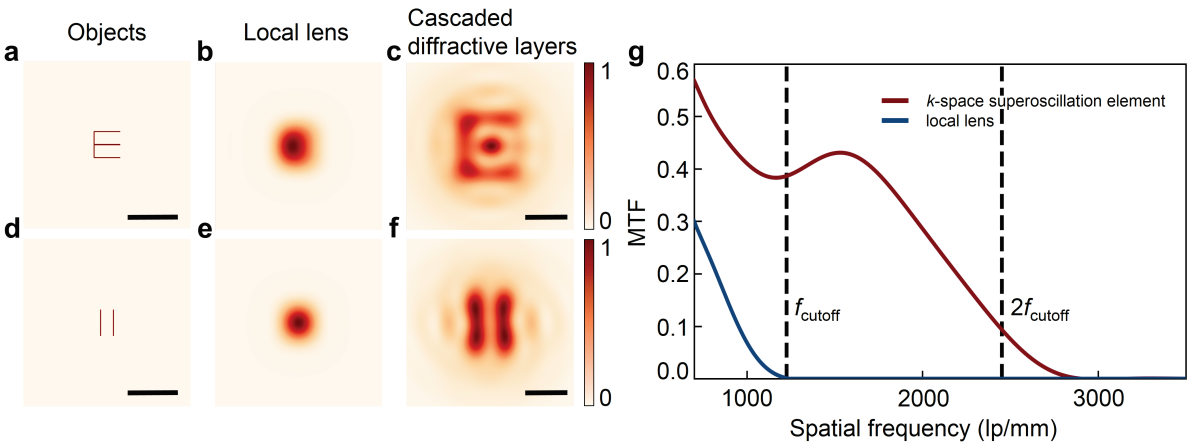



**Fig. S14 Cascaded refractive-diffractive superresolution imaging demonstration. a** The target object of letter 'E' with line spacing set to half the diffraction limit. Scale bar: 2 μm. **b-c** Simulated imaging results of a letter 'E' for the cascaded configuration with a local lens (**b**) and the nonlocal *k*-space superoscillation cascaded diffractive layers (c). Scale bar: 25 μm. **d** The target object of a double-slit with spacing set to half the diffraction limit. Scale bar: 2 μm. **e-f** Simulated imaging results of the double-slit obtained with the cascaded configuration using a conventional local lens (**e**) and the nonlocal *k*-space superoscillation cascaded diffractive layers (**f**). Scale bar: 25 μm. **g** Comparative MTFs of local lens and *k*-space superoscillation element.

Building upon the four-layer design, we have conducted additional simulations to explicitly evaluate its optical performance at a wavelength of 1550 nm. Our results demonstrate a lateral FOV of 4.90 μm with sidelobes consistently below 0.3 of the peak intensity. Furthermore, Fig. S15 presents simulated PSF line profiles across the FOV and quantifies the depth of focus (DoF). Specifically, the axial FWHM of the PSF at chief-ray angle $\theta = 0°$ defines the DoF of 919.9 μm.

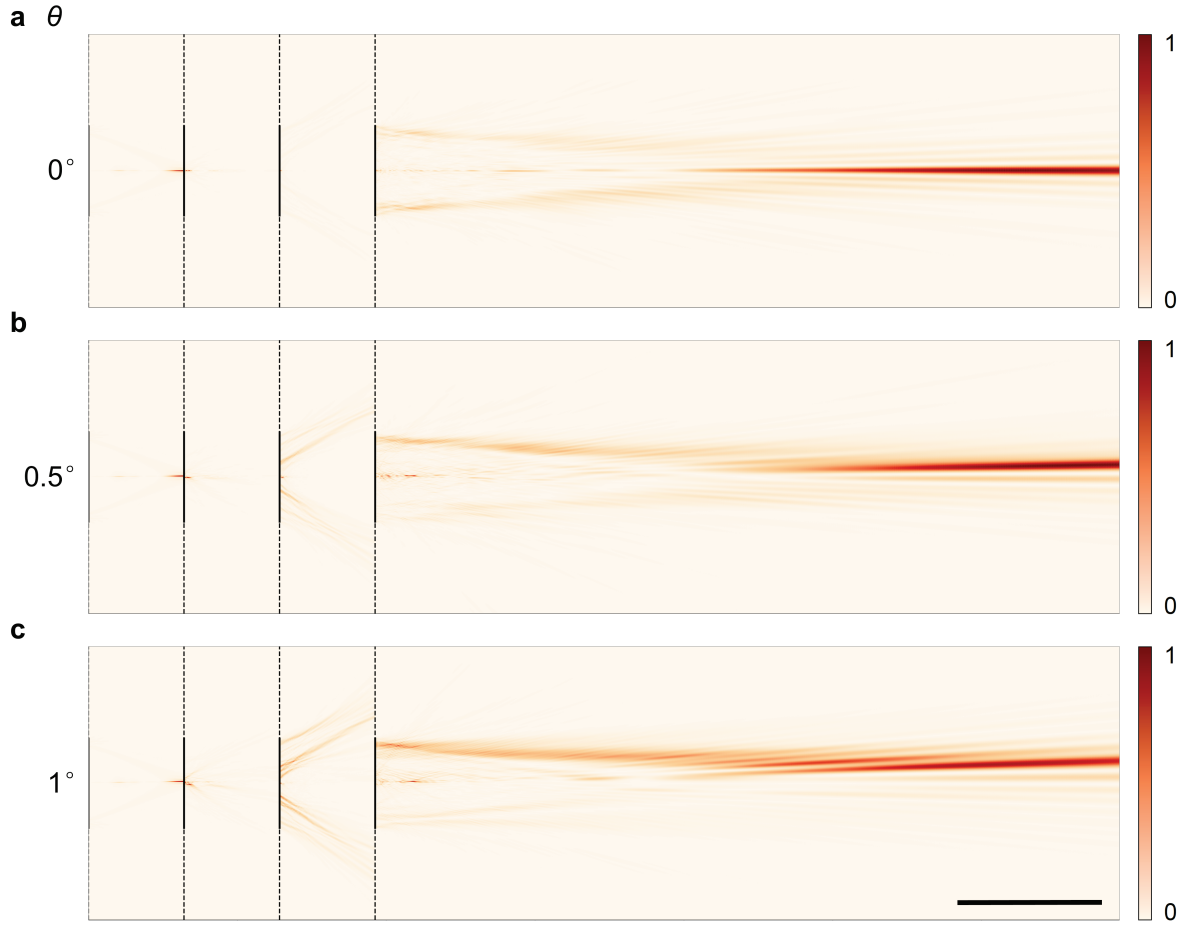



**Fig. S15 Optical performance of the *k*-space superoscillation cascaded diffractive layers.** Intensity profiles of the PSFs in the meridional plane from the first cascaded diffractive layer to the image plane, corresponding to chief-ray angles $\theta = 0°$, 0.5°, and 1°, respectively. The intensity distributions are normalized segment-wise between adjacent planes. Dashed lines indicate the positions of the cascaded diffractive layers, and solid lines mark the lateral extent

of these modulation elements. Scale bar, 200 μm.

To evaluate the tolerances of the cascaded diffractive layers, we simulated the SR under different phase errors and layer misalignments. Figure S16a shows the simulated average SR as a function of the phase errors, where the horizontal axis represents the error range characterized by three times the standard deviation of the added Gaussian noise as a percentage of the 2π phase modulation. The error bars represent the varying range of SRs across the FOV. The results indicate that the device exhibits tolerance with only a slight performance degradation with a fabrication error of up to 4%, corresponding to a depth error of approximately 120 nm. This tolerance requirement can be satisfied by modern nanofabrication techniques, which have been demonstrated to control phase errors to be around 2% or even lower [43, 49, 50].

In addition, Figure S16b illustrates the SR as a function of misalignment, expressed as a percentage of the pixel size (875 nm). The results indicate that the designed cascaded layers exhibit high robustness, showing only slight resolution degradation for misalignments up to 100% of the pixel size. Established methods employing alignment marks [40] are capable of achieving sub-pixel alignment accuracy. Furthermore, tolerances for both phase errors and layer misalignment could be further improved by adding regularization terms related to tolerance in the optimization process.

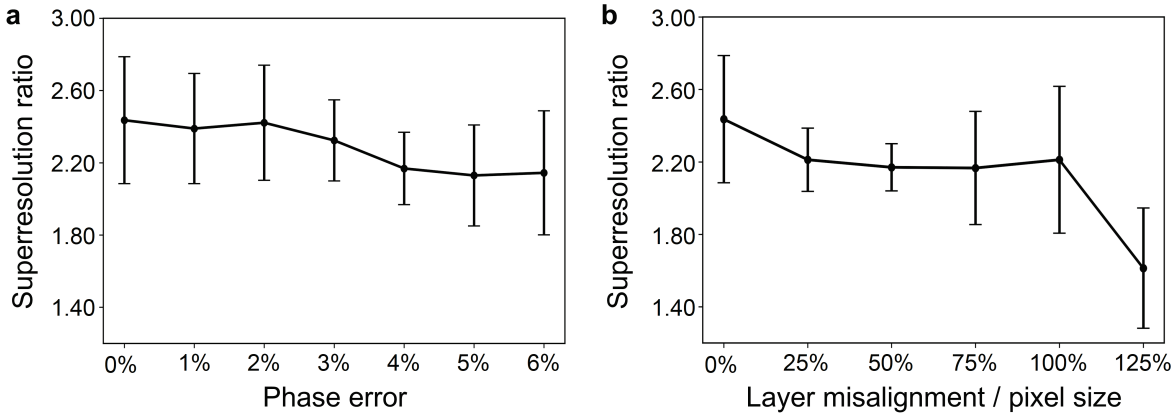



**Fig. S16 Tolerance analysis of the *k*-space superoscillation cascaded diffractive layers. a** Superresolution ratio as a function of the phase error. The phase errors are defined as three times the standard deviation of the added Gaussian noise relative to the 2π phase modulation. **b** Superresolution ratio as a function of layer misalignment. Error bars represent the varying range of superresolution ratios across the FOV.

## 15 1D large-scale optimization

To demonstrate that a large-scale superresolution metalens is achievable with sufficient computational resources, we optimized a 1D nonlocal volumetric metalens for transverse-magnetic (TM) polarized incidence—characterized by nonzero field components $E_x$, $H_y$, $H_z$ (see the x-y-z coordinate system in Fig. S17a)—with a FOV of ±1.91°. The 2D nonlocal metalens was made of 100 layers of polypropylene sheets (index = 1.5) with an element size of $0.2\lambda \times 0.2\lambda$. It comprised 500 × 100 elements with a total size of $100\lambda \times 20\lambda$. Fig. S17a shows optimized metalens structure. Using a point source placed at an infinite distance from the metalens, with the image plane located $125\lambda$ behind the output aperture, the PSF as a function of the incident angle can be calculated using the angular spectrum method from the simulated transmitted fields for both the 1D ideal response and the nonlocal metalens, as illustrated in Fig. S17b,c.

By comparing the ratio $\Delta r_p/\Delta r_m$ of the 1D nonlocal metalens to that of the ideal response, a SR ranging from 1.72 to 2.20 can be obtained across the FOV. Besides, by calculating the angle-dependent transmitted field distribution of the 1D metalens and performing a Fourier transform on $k_x$, we verified that the local change rate within the FOV exceeds the range of the aperture $D$ shown as the blue dashed line in Fig. S17d. For the overall angular range, since $T(x', k_x)$ inside and outside the FOV cancel each other out outside the input aperture, there is no violation of the restriction that the overall bandwidth is limited by the aperture size (Fig. S17e). This reflects that, from the perspective of Fourier optics, the nonlocal metalens does not require angular-spectrum components beyond the aperture limit, but instead reshapes and coherently reweights the received spectrum within the aperture to realize superresolution imaging. The optimized distribution (Fig. S17d) differs from the idealized analytical form (Fig. 1f), as the latter represents one conceptual form and is not the only feasible solution. The topology optimization space was enlarged by treating the PSF phase as an additional optimization parameter, while the degrees of freedom were limited by fabrication constraints.

Without any post-processing, the 1D local lens resolves four points at an angular separation of 0.63° with a valley-to-peak ratio of 0.81 (the second row in Fig. S18b). In comparison, the 1D nonlocal metalens resolves four points at an angular separation of 0.41° with the valley-to-peak ratio of 0.81 (the third row in Fig. S18c), indicating that the resolution of the nonlocal metalens is 1.54 times higher than that of the local lens. The sidelobes present in the directly captured 1D images can be suppressed using a spatially-varying deconvolution algorithm as well. With the known spatially-varying PSF and an initial guess of the target object, the difference between the measured and theoretically estimated data can be iteratively minimized to achieve superresolution imaging with reduced sidelobes. Fig. S18d shows the results of the deconvolution with 10 dB Gaussian noise added to the superimposed image, indicating that the spatially-varying deconvolution algorithm can effectively suppress sidelobes

for multiple objects.

The normalized FOV of this large-scale 1D nonlocal metalens is notably larger than the corresponding value reported in the main text. This highlights that increased design freedom and computational resources enable enhancement of the achievable FOV. Beyond optimizing a single element, practical approaches to further enlarging the effective FOV involve arrayed or scanning imaging strategies. Specifically, one could employ a mosaic arrangement of multiple nonlocal *k*-space superoscillation elements, each covering a subregion of the total desired field, or alternatively scan either the object or lens relative to each other to stitch together multiple partial images. Both strategies inherently enable maintaining the designed resolution while covering a substantially expanded scene.

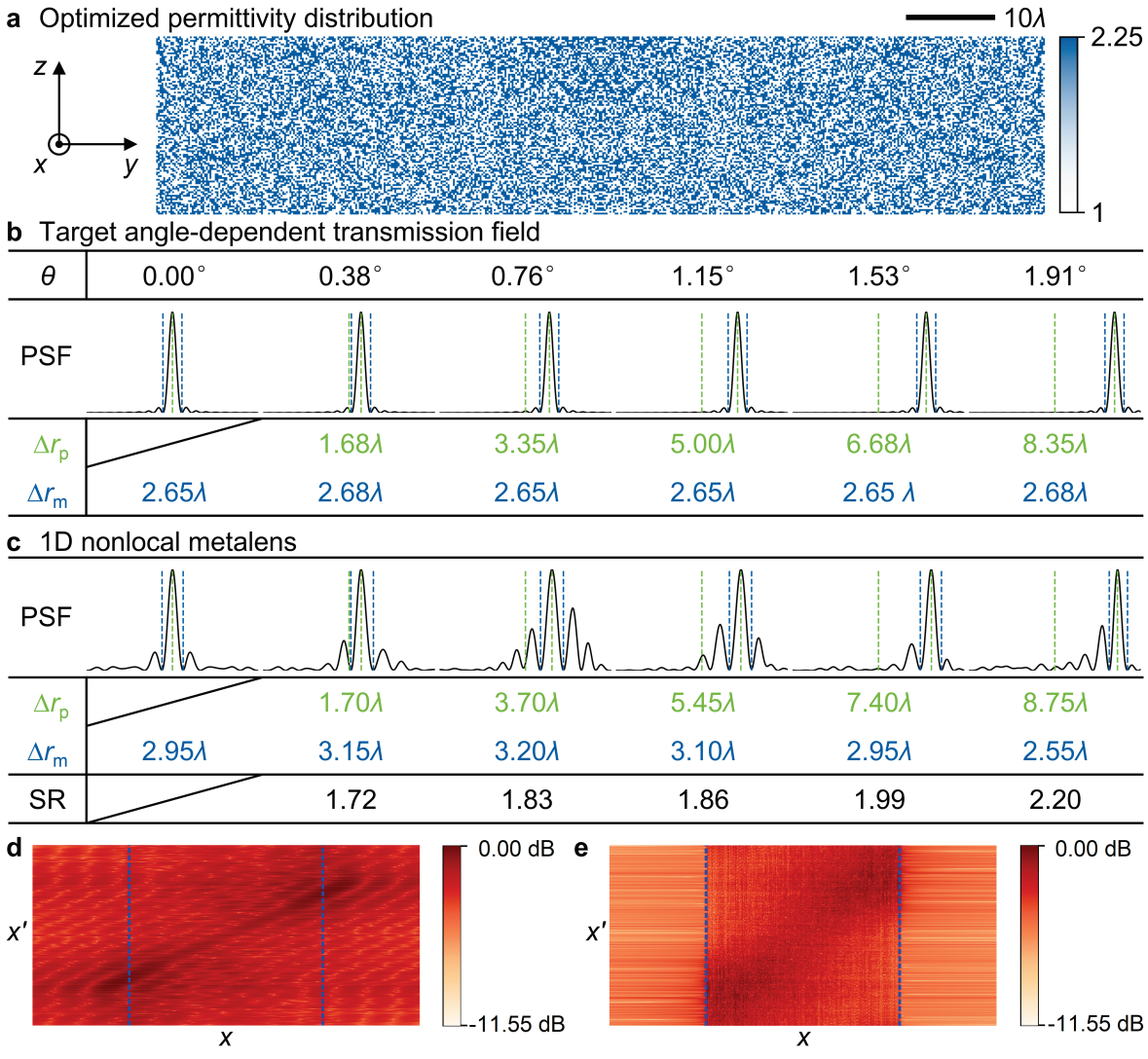


**Fig. S17 Larger-scale 1D metalens design and optimization. a** Optimized 1D metalens structure. **b** Simulated PSF as a function of the angular position of the point source calculated from the transmitted field using the ASM for the 1D ideal response with double lateral magnification of perfect imaging. **c** Simulated PSF as a function of the angular position of the point source calculated from the transmitted field using the ASM for the optimized 1D nonlocal metalens. SR, superresolution ratio. **d** The common logarithm of intensity distribution of local transmission function within the FOV. The dashed line shows the range of the input aperture. **e** The common logarithm of intensity of transmission function for all incident angles. The dashed line shows the range of the input aperture.

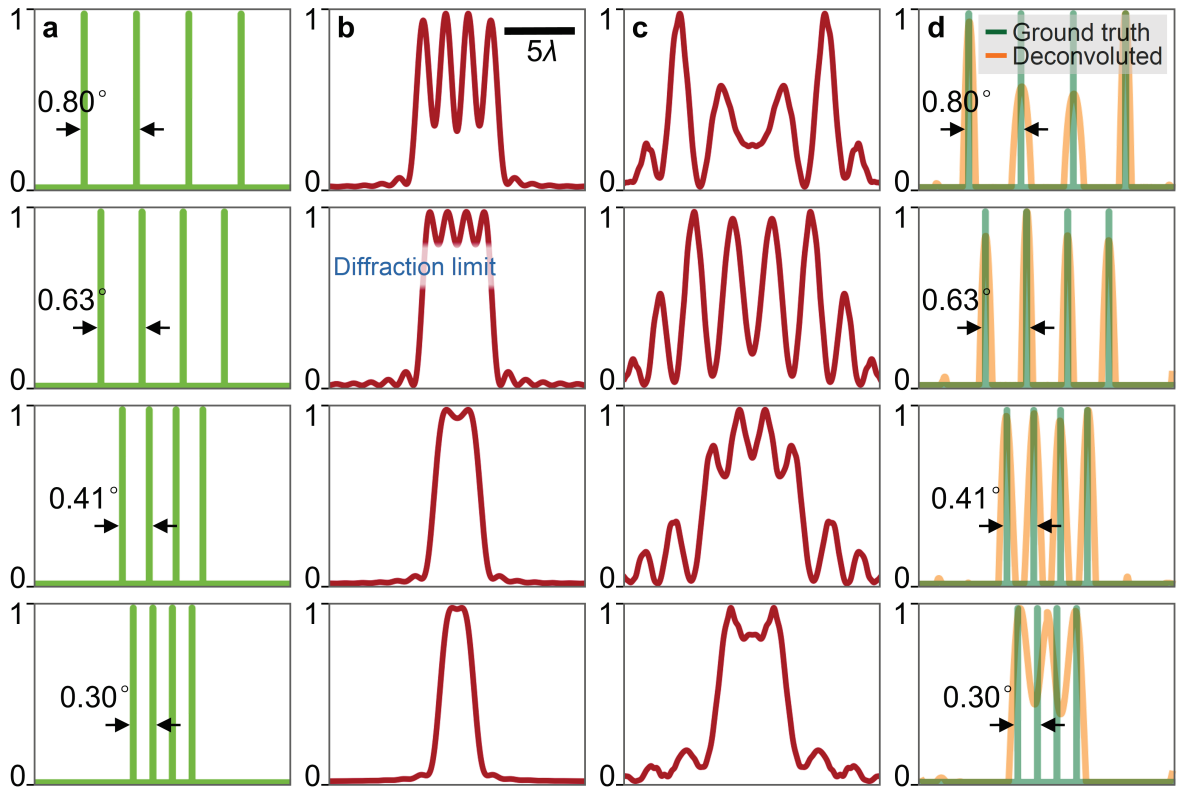



**Fig. S18 Imaging multiple objects using the 1D nonlocal metalens. a** Target object of four-point sources at distances ranging from 0.30° to 0.80°. **b** Images directly captured by a 1D local lens. **c** Images directly captured by the optimized 1D nonlocal metalens. **d** Reconstructed

images with suppressed sidelobes using spatially-varying deconvolution from images directly captured from the nonlocal metalens.

## References


1. J. W. Goodman, Introduction to Fourier Optics (Roberts & Company Publishers, Greenwood Village, 2005).
2. K. Huang, H. Ye, J. Teng, S.P. Yeo, B. Luk'yanchuk, C.W. Qiu, Optimization-free superoscillatory lens using phase and amplitude masks. Laser & Photonics Reviews **8**, 152-157 (2014).
3. F. Qin, K. Huang, J. Wu, J. Teng, C.W. Qiu, M. Hong, A Supercritical Lens Optical Label-Free Microscopy: Sub-Diffraction Resolution and Ultra-Long Working Distance. Advanced Materials **29**, 1602721 (2017).
4. Z. Lin, C. Roques-Carmes, R.E. Christiansen, M. Soljačić, S.G. Johnson, Computational inverse design for ultra-compact single-piece metalenses free of chromatic and angular aberration. Applied Physics Letters **118**, 041104 (2021).
5. H. Liu, Y. Yan, Q. Tan, G. Jin, Theories for the design of diffractive superresolution elements and limits of optical superresolution. Journal of the Optical Society of America **19**, 2185-2193 (2002).
6. E.T. Rogers, J. Lindberg, T. Roy, S. Savo, J.E. Chad, M.R. Dennis, N.I. Zheludev, A super-oscillatory lens optical microscope for subwavelength imaging. Nature Materials **11**, 432-435 (2012).
7. G. Yuan, K.S. Rogers, E.T.F. Rogers, N.I. Zheludev, Far-Field Superoscillatory Metamaterial Superlens. Physical Review Applied **11**, 064016 (2019).
8. M.V. Berry, Five momenta. European Journal of Physics **34**, 1337-1348 (2013).
9. M.V. Berry, P. Shukla, Pointer supershifts and superoscillations in weak measurements. Journal of Physics A: Mathematical and Theoretical **45**, 015301 (2012).
10. M.V. Berry, S. Popescu, Evolution of quantum superoscillations and optical superresolution without evanescent waves. Journal of Physics A: Mathematical and General **39**, 6965-6977 (2006).
11. H. Yang, E.Y.H. Lin, K.N. Kutulakos, G.V. Eleftheriades, Sub-wavelength passive single-shot computational super-oscillatory imaging. Optica **9**, 1444-1447 (2022).
12. L. Wang, A. H. C. Ng, and K. Deb (ed.), Multi-objective Evolutionary Optimisation for Product Design and Manufacturing (Springer, London, 2011).
13. M.V. Berry, Suppression of superoscillations by noise. Journal of Physics A: Mathematical and Theoretical **50**, 025003 (2017).
14. K.S. Rogers, K.N. Bourdakos, G.H. Yuan, S. Mahajan, E.T.F. Rogers, Optimising superoscillatory spots for far-field super-resolution imaging. Optics Express **26**, 8095-8112 (2018).
15. N.I. Zheludev, G. Yuan, Optical superoscillation technologies beyond the diffraction limit. Nature Reviews Physics **4**, 16-32 (2022).

16. H.C. Lin, Z. Wang, C.W. Hsu, Fast multi-source nanophotonic simulations using augmented partial factorization. Nature Computational Science **2**, 815-822 (2022).
17. F. Wang, B.S. Lazarov, O. Sigmund, On projection methods, convergence and robust formulations in topology optimization. Structural and Multidisciplinary Optimization **43**, 767-784 (2011).
18. K. Svanberg, A Class of Globally Convergent Optimization Methods Based on Conservative Convex Separable Approximations. SIAM Journal on Optimization **12**, 555-573 (2002).
19. K.H. Brenner, W. Singer, Light propagation through microlenses: a new simulation method. Applied Optics **32**, 4984-4988 (1993).
20. G.H. Yuan, N.I. Zheludev, Detecting nanometric displacements with optical ruler metrology. Science **364**, 771-775 (2019).
21. A.M.H. Wong, G.V. Eleftheriades, Sub-Wavelength Focusing at the Multi-Wavelength Range Using Superoscillations: An Experimental Demonstration. IEEE Transactions on Antennas and Propagation **59**, 4766-4776 (2011).
22. Z. Wu, J. Zhu, Y. Zou, H. Deng, L. Xiong, Q. Liu, L. Shang, Superoscillatory metalens for polarization conversion and broadband tight focusing of terahertz waves. Optical Materials **123**, 111924 (2022).
23. J. Li, G. Yang, Y. Yuan, Q. Wu, K. Zhang, Ultra-Thin Chiral Metasurface-Based Superoscillatory Lens. Frontiers in Materials **8**, 806725 (2022).
24. C. Wang, D. Tang, Y. Wang, Z. Zhao, J. Wang, M. Pu, Y. Zhang, W. Yan, P. Gao, X. Luo, Super-resolution optical telescopes with local light diffraction shrinkage. Scientific Reports **5**, 18485 (2015).
25. D. Tang, C. Wang, Z. Zhao, Y. Wang, M. Pu, X. Li, P. Gao, X. Luo, Ultrabroadband superoscillatory lens composed by plasmonic metasurfaces for subdiffraction light focusing. Laser & Photonics Reviews **9**, 713-719 (2015).
26. G.H. Yuan, E.T. Rogers, N.I. Zheludev, Achromatic super-oscillatory lenses with sub-wavelength focusing. Light: Science & Applications **6**, e17036 (2017).
27. V.V. Kotlyar, A.G. Nalimov, S.S. Stafeev, C. Hu, L. O'Faolain, M.V. Kotlyar, D. Gibson, S. Song, Thin high numerical aperture metalens. Optics Express **25**, 8158-8167 (2017).
28. R. Zuo, W. Liu, H. Cheng, S. Chen, J. Tian, Breaking the Diffraction Limit with Radially Polarized Light Based on Dielectric Metalenses. Advanced Optical Materials **6**, 1800795 (2018).
29. K.S. Rogers, E.T.F. Rogers, Realising superoscillations: A review of mathematical tools and their application. Journal of Physics: Photonics **2**, 042004 (2020).
30. A. Grbic, G.V. Eleftheriades, Overcoming the diffraction limit with a planar left-handed transmission-line lens. Physical Review Letters **92**, 117403 (2004).
31. P.A. Belov, Y. Hao, S. Sudhakaran, Subwavelength microwave imaging using an array of parallel conducting wires as a lens. Physical Review B **73**, 033108 (2006).
32. R. Schmidt, Multiple emitter location and signal parameter estimation. IEEE Transactions on Antennas and Propagation **34**, 276-280 (1986).
33. M.A. Herman, T. Strohmer, High-Resolution Radar via Compressed Sensing. IEEE Transactions on Signal Processing **57**, 2275-2284 (2009).
34. A. Shayei, Z. Kavehvash, M. Shabany, Improved-resolution millimeter-wave imaging through structured illumination. Applied Optics **56**, 4454-4465 (2017).

35. W. Li, J. Qi, A. Alu, Single-pixel super-resolution with a space–time modulated computational metasurface imager. Photonics Research **12**, 2311-2322 (2024).
36. X.H. Dong, A.M.H. Wong, M. Kim, G.V. Eleftheriades, Superresolution far-field imaging of complex objects using reduced superoscillating ripples. Optica **4**, 1126-1133 (2017).
37. X. Luo, F. Zhang, M. Pu, Y. Guo, X. Li, X. Ma, Recent advances of wide-angle metalenses: principle, design, and applications. Nanophotonics **11**, 1-20 (2021).
38. M. Pan, Y. Fu, M. Zheng, H. Chen, Y. Zang, H. Duan, Q. Li, M. Qiu, Y. Hu, Dielectric metalens for miniaturized imaging systems: progress and challenges. Light: Science & Applications **11**, 195 (2022).
39. H. Yu, Z. Huang, S. Lamon, B. Wang, H. Ding, J. Lin, Q. Wang, H. Luan, M. Gu, Q. Zhang, All-optical image transportation through a multimode fibre using a miniaturized diffractive neural network on the distal facet. Nature Photonics **19**, 486–493 (2025).
40. H. Chen, J. Feng, M. Jiang, Y. Wang, J. Lin, J. Tan, P. Jin, Diffractive Deep Neural Networks at Visible Wavelengths. Engineering **7**, 1483-1491 (2021).
41. B. Xu, H. Li, S. Gao, X. Hua, C. Yang, C. Chen, F. Yan, S. Zhu, T. Li, Metalens-integrated compact imaging devices for wide-field microscopy. Advanced Photonics **2**, 066004 (2020).
42. J. Duparre, P. Schreiber, A. Matthes, E. Pshenay-Severin, A. Brauer, A. Tunnermann, R. Volkel, M. Eisner, T. Scharf, Microoptical telescope compound eye. Optics Express **13**, 889-903 (2005).
43. E. Goi, X. Chen, Q. Zhang, B.P. Cumming, S. Schoenhardt, H. Luan, M. Gu, Nanoprinted high-neuron-density optical linear perceptrons performing near-infrared inference on a CMOS chip. Light: Science & Applications **10**, 40 (2021).
44. E. Goi, S. Schoenhardt, M. Gu, Direct retrieval of Zernike-based pupil functions using integrated diffractive deep neural networks. Nature Communications **13**, 7531 (2022).
45. S. Kawata, H.-B. Sun, T. Tanaka, K. Takada, Finer features for functional microdevices. Nature **412**, 697-698 (2001).
46. M. Emons, K. Obata, T. Binhammer, A. Ovsianikov, B.N. Chichkov, U. Morgner, Two-photon polymerization technique with sub-50 nm resolution by sub-10 fs laser pulses. Optical Materials Express **2**, 942-947 (2012).
47. L. Zheng, K. Kurselis, A. El-Tamer, U. Hinze, C. Reinhardt, L. Overmeyer, B. Chichkov, Nanofabrication of High-Resolution Periodic Structures with a Gap Size Below 100 nm by Two-Photon Polymerization. Nanoscale Research Letters **14**, 134 (2019).
48. X. Lin, Y. Rivenson, N.T. Yardimci, M. Veli, Y. Luo, M. Jarrahi, A. Ozcan, All-optical machine learning using diffractive deep neural networks. Science **361**, 1004-1008 (2018).
49. M.B. Stern, M. Holz, S.S. Medeiros, R.E. Knowlden, Fabricating binary optics: Process variables critical to optical efficiency. Journal of Vacuum Science & Technology B: Microelectronics and Nanometer Structures Processing, Measurement, and Phenomena **9**, 3117-3121 (1991).
50. M. Davanco, L. Yu, L. Chen, V. Luciani, J.A. Liddle, Assessing fabrication tolerances for a multilevel 2D binary grating for 3D multifocus microscopy. Optics Express **24**, 9224-9236 (2016).